

# Offshore and Onshore Power curve characterization for ground-generation AWES

Markus Sommerfeld<sup>1</sup>, Martin Dörenkämper<sup>2</sup>, Jochem De Schutter<sup>3</sup>, and Curran Crawford<sup>1</sup>

<sup>1</sup>Institute for Integrated Energy Systems, University of Victoria, British Columbia, Canada

<sup>2</sup>Fraunhofer Institute for Wind Energy Systems, Oldenburg, Germany

<sup>3</sup>Systems Control and Optimization Laboratory IMTEK, Freiburg, Germany

**Correspondence:** Markus Sommerfeld (msommerf@uvic.ca)

## Abstract.

Airborne wind energy systems (AWESs) are nominally envisaged to operate at altitudes above conventional wind turbines (WTs) and harvest energy from stronger winds aloft. This study investigates typical flight trajectories, operating heights, power curves and annual energy production (AEP) of a ground-generation AWES with a wing area of  $A_{wing} = 20\text{m}^2$ . Various companies and researchers have proposed power curve characterizations for AWES, but no consensus for an industry-wide standard has been reached. A universal description of a ground-generation AWES power curve is difficult to define, because of complex tether and misalignment losses subject to alternating flight paths and wind conditions, which lead to significant changes in the average cycle power. This study determines AWES power and AEP based on the `awebox` optimal control model driven by representative onshore and offshore wind data. 10-minute mesoscale onshore and offshore wind conditions are analyzed and categorized with respect to atmospheric stability as well as annual and diurnal variation. To reduce computational costs, these wind data are categorized using k-means clustering. The derived profiles cover a wide range of wind speeds and profile shapes which can not be replicated by standard logarithmic wind speed profiles. Wind data drives the optimization and result in distinct optimal AWES trajectories and power cycles.

Our data shows that optimal AWES operating heights are generally below 400 m and mostly around 200 m. We compare AWES power curve descriptions and estimate AEP based on wind speed probability distributions over various reference heights. These results are compared to quasi steady-state (QSS) AWES and WT reference models. The optimized power curves show a delay in rated wind speed which can be attributed to increased tether losses which are not captured by the simplified model. Offshore AEP is generally higher than onshore, but lower wind shear weakens the argument for higher operating altitudes for AWES compared to conventional WT.

## 20 1 Introduction

Airborne wind energy systems (AWESs) aspire to harvest stronger and less turbulent winds at mid-altitude, here defined as heights above 100 m and below 1500 m, nominally beyond what is achievable with conventional wind turbines (WTs). The prospects of higher energy yield combined with reduced capital cost motivate the development of this novel class of renewable energy technology (Lunney et al., 2017; Fagiano and Milanese, 2012). Unlike conventional WT, which have converged to

25 a single concept with three blades and a conical tower, several different AWES concepts and designs are under investigation  
by numerous companies and research institutes (Cherubini et al., 2015). These kite-inspired systems consist of three main  
components: one or more flying wings or kites, one or more ground stations and one or more tethers to connect them. This  
study focuses on the two-phase, ground-generation concept, also referred to as pumping-mode, which is the main concept  
30 which is connected to a generator, thereby producing electricity. This is then followed by the reel-in phase during which the  
wing adjusts its angle of attack to reduce aerodynamic forces and returns to its initial position. Various other concepts such as  
fly-gen, aerostat or rotary lift are not within the scope of this study (Cherubini et al., 2015).

Since this technology is still at an early stage of development, validation and comparison of results is difficult. A standard-  
ized power curve definition would enable comparison between different AWES concepts and to conventional wind turbines.  
35 Together with the site-specific wind resource, power curves help wind park planners and AWES device manufacturers to es-  
timate annual energy production (AEP) and determine financial viability (Malz et al., 2020). Note that the wind data used to  
derive the AEP estimates are not fully, in accordance with wind resource assessment guidelines which typically recommend  
multi-year wind measurements and long-term wind data corrections via simulations. All statements made in this research only  
apply to the investigated time periods and locations which are assumed to be reasonable representative of wind profiles that  
40 would be encountered during operation (Section 2). This work supports the development and implementation  
of this novel technology by proposing a methodology to estimate power and energy generation based on a small set of real-  
istic wind conditions. In contrast to a conventional WT, the power output of an AWES is highly dependent on the complete  
wind speed profile (wind speed and direction variation with height) as system performance is governed by optimal operating  
trajectories over the wind profile altitude range rather than primarily by a hub-height wind speed. Simple wind profile approxi-  
45 mations using logarithmic or exponential wind speed profiles, which are often erroneously applied beyond earths surface layer  
(Optis et al., 2016), might approximate long-term average conditions, but can not capture the broad variation of profile shapes  
that exist on short timescales (Emeis, 2018). They are therefore an inappropriate approximation to estimate instantaneous,  
diurnal and seasonal variation in electrical power output. However, they are the standard in most AWES power estimation  
studies. (Leuthold et al., 2018) investigated the power-optimal trajectories and performance of a ground-generation multiple-  
50 kite AWES over a range of logarithmic wind speed profiles, with different reference wind speeds. In (Licitra et al., 2019) the  
authors estimate the performance and power curve of a ground-generation, rigid wing AWES by generating power-optimal  
trajectories and validate against Ampyx AP2 data. The optimal, single-loop trajectories are defined by a simple power law  
approximation of the wind speed profile. Because of the the up-scaling drawbacks of single-kite AWES, (De Schutter et al.,  
2019) analyzes the performance of utility-scale, stacked multi-kite systems, using the same optimization framework as this  
55 research. Two logarithmic wind speed profiles, one onshore and one offshore, provide boundary conditions for the non-linear  
optimization problem. Aull et al.(Aull et al., 2020) explore the design and size of fly-gen rigid wing AWES based on a steady-  
state model with simple aerodynamic and mass scaling approximations. The wind resource is described by an exponential wind  
shear model with Weibull distribution. (Leuthold et al., 2018; Licitra et al., 2019; De Schutter et al., 2018; Aull et al., 2020) An  
alternative approach to estimating AWES energy production using the Dutch Offshore Wind Atlas, LiDAR and ERA5 global

60 reanalysis wind data set can be found in (Schelbergen et al., 2020a). The authors use principal component analysis and k-means clustering to determine representative wind speed profiles for a part of the Netherlands and the North Sea.

AWES need to dynamically adapt their flight trajectory to changing winds in order to optimize power production. Wind velocity profiles are governed by environmental, location-dependent conditions (e.g. surface roughness) and weather phenomena on a multitude of temporal and spatial scales, subject to diurnal and seasonal patterns. The preferable means of determining  
65 wind conditions are long-term, high resolution measurements, which at mid-altitudes can solely be achieved by long-range light detection and ranging (LiDAR). Numerical mesoscale weather prediction models such as the weather research and forecasting model (WRF), which is well known for conventional WT siting applications (Salvação and Guedes Soares, 2018; Dörenkämper et al., 2020), are used to estimate wind conditions on time scales of a few minutes to years. These numerical simulations should be corrected for systematic errors using measurements from LiDAR during site assessment and deployment as well as  
70 multi-year, long-term wind simulations. An investigation using simulated long-term wind statistics is beyond the scope of this paper. Measuring wind conditions at mid-altitudes is costly and difficult, due to reduced data availability (Sommerfeld et al., 2019a). Additionally, measurements are hard to find, because they are typically proprietary. Therefore, wind data in this study are exclusively based on uncorrected WRF mesoscale simulations (Skamarock et al., 2008). The same trajectory optimization methodology can be applied to any wind data, but is here illustrated with WRF data. We compare conventional WT hub-height  
75 based power curves to optimal AWES performance for an onshore location in northern Germany near the city of Pritzwalk (Sommerfeld et al., 2019b) and an offshore location at the FINO3 research platform in the North Sea.

The key contribution of this paper is the derivation and analysis of optimal AWES performance, operating height, trajectory, power and AEP, based on a dynamic optimization model, subject to realistic wind profiles. Another goal is to illustrate the problem of describing AWES power curves and estimating annual energy prediction, because no to agreed upon standard wind  
80 conditions or reference height exist. We compare the impact of different reference heights and propose a proxy for AWES operating height as a proxy. This is achieved by clustering the simulated wind velocity vectors using k-means clustering. Optimizing the AWES trajectories only for a representative subset of profiles reduces the computational cost significantly, while maintaining important wind profile characteristics. Results from the `awebox` optimization framework are compared to a quasi steady-state reference model. The impact of wind data is visualized by comparing results based on optimized trajectories  
85 to a quasi steady-state AWES model.

In summary, this manuscript provides insight into typical onshore and offshore wind conditions up to 1000 m, their variation and the potential application of clustering to identify representative wind speed profiles and in turn yield more realistic AWES power and energy estimation. Firstly, the wind resource and its underlying wind model are described. The model data is then categorized into several clusters and selected wind profiles are implemented into an optimization framework to determine  
90 power-optimal trajectories. Results are then referenced against a quasi steady-state AWES model, subject to the same wind profiles.

Section 2 introduces the mesoscale WRF model set-up and compares the onshore and offshore wind resource. Section 3 introduces the k-means clustering algorithm and summarizes results of clustered wind velocity profiles (both longitudinal and lateral wind components). These include cluster-averaged profiles and correlation with seasonal, diurnal and atmospheric

95 stability. Section 5.1 introduces the `awebbox` optimization framework. It summarizes aircraft, tether and ground station models  
as well as system constraints and initialization used to produce the results shown in Section 6. These include flight paths and  
time series of various performance parameters, and a statistical analysis of tether length and operating altitude. Furthermore, we  
compare power curve characterization, capacity factor and AEP estimates. Based on these results, an AWES power coefficient  
is defined to approximate AWES efficiency and power based on system size and wind speed. Finally, Section 7 concludes with  
100 an outlook and motivation for future work.

## 2 Wind conditions

This study compares the general AWES performance and power curves at a representative onshore and offshore location in  
Europe (fig 1). Wind conditions for the chosen years are assumed to be representative of that location. The comparison and  
implementation of long-term data from wind atlases is beyond the scope of this research. The “Onshore” wind data at the  
105 Pritzwalk Sommersberg airport (lat:  $53^{\circ}10'47.00''\text{N}$ , lon:  $12^{\circ}11'20.98''\text{E}$ ) in northern Germany and comprises 12 months of  
WRF simulation data between September 2015 and September 2016. The area surrounding the airport mostly consists of flat  
agricultural land with the town of Pritzwalk to the south and is therefore a fitting location for wind energy generation (see  
(Sommerfeld et al., 2019a) and (Sommerfeld et al., 2019b) for details). The FINO3 research platform in the North Sea (lat:  
 $55^{\circ}11,7'\text{N}$ , lon:  $7^{\circ}9,5'\text{E}$ ) was chosen as a representative “offshore” location due to the proximity to several offshore wind  
110 farms and the amount of comprehensive reference measurements (Peña et al., 2015). The offshore simulation covers the time  
frame between September 2013 and September 2014.

### 2.1 Mesoscale model

The mesoscale simulations in this study were carried out using the weather research and forecasting (WRF) model from  
(Skamarock et al., 2008). The onshore simulation was performed with version 3.6.1 (Skamarock et al., a) before the 2018  
115 release of WRF version 4.0.2 (Skamarock et al., b, c) in which the offshore simulations were computed. The setup of the  
model has been adapted and constantly optimized for wind energy applications by the authors with the framework of various  
projects and applications in recent years (Dörenkämper et al., 2015, 2017; Dörenkämper et al., 2020; Hahmann et al., 2020;  
Sommerfeld et al., 2019b).

The focus of this study is not on the detailed comparison between mesoscale models, but on AWES performance subject  
120 to representative onshore and offshore wind conditions determined based on clustered wind profiles (described in Section 3).  
Both WRF models provide adequate wind data for for the assessment of AWES performance, even though the setup and time  
frame are different.

Both simulations consist of three nested domains centered around either the FINO3 met mast (Figure 1) or the Pritzwalk  
Sommersberg airport. Atmospheric boundary conditions are defined by ERA-Interim (Dee et al., 2011) for the onshore location  
125 and by ERA5 (Hersbach and Dick, 2016) reanalysis data for the offshore location, while sea surface parameters for the offshore  
location are based on OSTIA (Donlon et al., 2012). These data sets have proven to provide good results for wind energy relevant

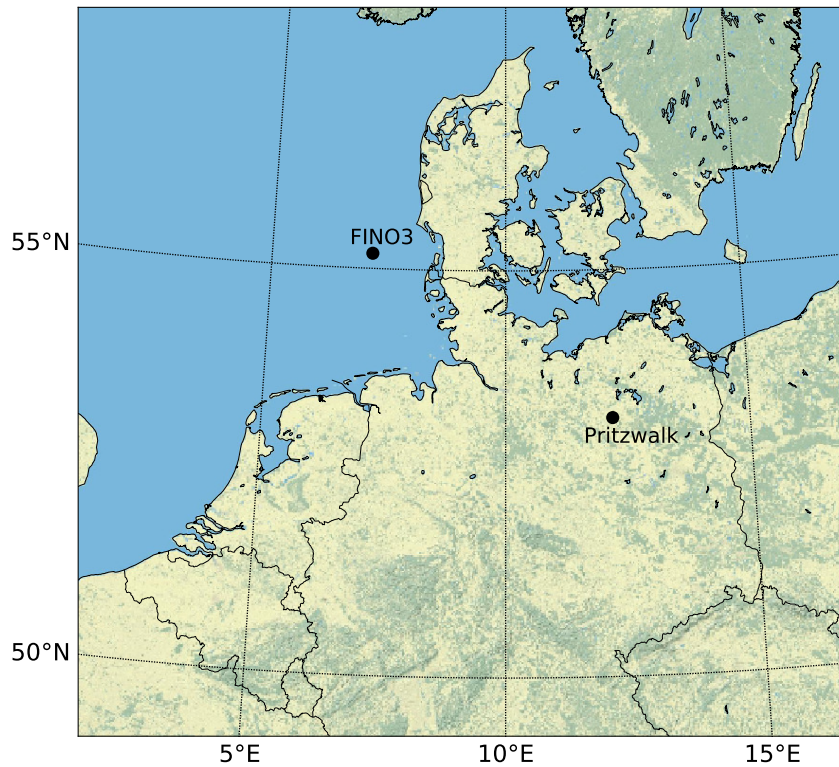


**Figure 1.** Map of northern Germany with the representative onshore (Pritzwalk) and offshore (FINO3) locations highlighted by black dots.

heights and sites (Olauson, 2018; Hahmann et al., 2020). Both simulations use the MYNN 2.5 level scheme for the planetary boundary layer (PBL) physics (Nakanishi and Niino, 2009). While the onshore simulation was performed in one 12 month simulations (01.09.2015 - 31.08.2016), the offshore simulation period consisted of 410 days (30.08.2013 - 14.10.2014) that were split into 41 simulations of 10 days each with an additional 24 hours of spin-up time per run. The data from the mesoscale models sigma levels (terrain-following) were transformed to the geometric heights using the post-processing methodology described in (Dörenkämper et al., 2020). Table 1 summarizes the key parameters of the model settings used in this study. All simulations were run on the *EDDY* High-Performance Computing clusters at the University of Oldenburg (Carl von Ossietzky Universität Oldenburg, 2018).

**Table 1.** Key setup parameters of the onshore and offshore mesoscale model simulations

Model Parameter	Settings	
	Onshore	Offshore
WRF model version	3.5.1	4.0.2
time period	01.09.2015 - 31.08.2016	30.08.2013 - 14.10.2014
Reanalysis	ERA-Interim	ERA5 & OSTIA
Horizontal grid size (D01, D02, D03)	120x120, 121x121, 121x121	150x150, 151x151 , 151x151
Resolution (D01, D02, D03)	27 km, 9 km, 3 km	18 km, 6 km, 2 km
Vertical levels	60 sigma levels (about 25 below 2 km)	60 sigma levels (about 25 below 2 km)
Nesting	1-way	1-way
Initialisation strategy	single run	240 h runs plus 24 h spinup time
Nudging	Analysis nudging (FDDA)	Analysis nudging (FDDA)
PBL scheme	MYNN level 2.5 scheme	MYNN level 2.5 scheme
Micro physics	Ferrier scheme	WRF Single–moment 5–class scheme
Long wave & shortwave radiation	RRTM & Dudhia	RRTMG scheme

## 135 2.2 Wind regime

Figure 2 depicts the wind roses of the annual wind conditions at 100 (top) and 500 m (bottom) height onshore (left) and offshore (right). The dominant wind direction at both locations is southwest, turning clockwise with increasing altitude.

Directional variability decreases and wind speed increases with height, following the expected trends in the northern hemisphere (Arya and Holton, 2001; Stull, 1988). The average onshore wind direction turns about 14° between 100 and 500 m, whereas average offshore wind direction only veers approximately 5°. The offshore wind direction turns approximately 10° additional degrees above 500 m, resulting in roughly the same westerly wind direction at high altitudes at around 1000 m. Due to prevailing unstable conditions offshore, a strong mixing with height is found resulting in less veer across the heights investigated in this study. The wind shear at the offshore location is lower compared to the onshore location due to lower surface roughness.

145 Figure 3 shows the annual horizontal wind speed probability distributions at each individual height level for both locations. These distributions give an insight into the wind speed statistics at individual heights, but not into the statistics of the wind profile shapes, which are important for AWES power and trajectory optimization. The chosen nonlinear color range allows for the representation of the entire relative probability range. Onshore (left) wind speeds are relatively low and have a fairly narrow range below 300 m, due to dominant surface effects. Above this height the distribution broadens, but a high probability of low  
150 wind speeds remains for the full height range. The distributions show bi-modal characteristics caused by different atmospheric

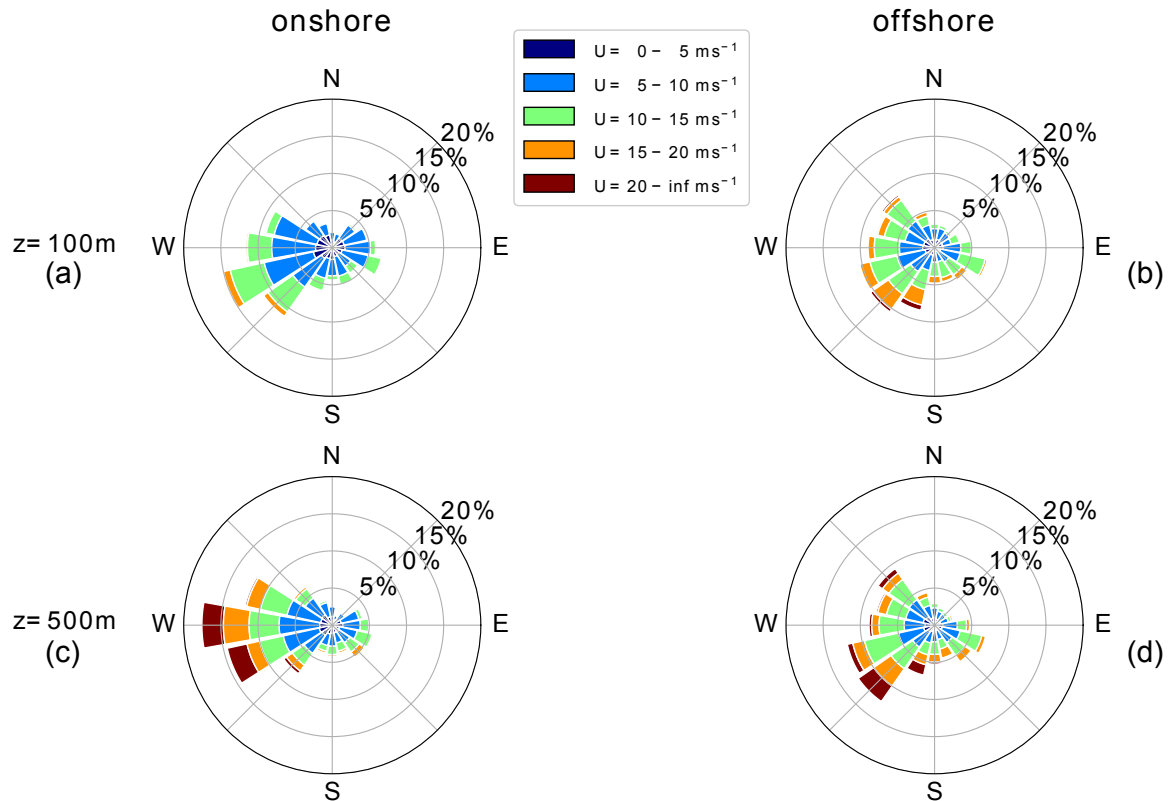


**Figure 2.** Annual wind direction and speed statistics at Pritzwalk (onshore) and FINO3 (offshore) presented as wind roses for 100 and 500 m.

stratification. Low wind speeds are commonly associated with unstable and high wind speeds with neutral or stable atmospheric conditions.

Such multimodal distributions at higher altitudes are better described by the sum of two or more probability distributions, as standard Weibull or Rayleigh distributions can not capture this phenomenon (Sommerfeld et al., 2019a). Offshore (right) wind speeds on the other hand have a wider distribution at all heights as they are less inhibited by surface effects. Similar to  
 155 wind speeds on the other hand have a wider distribution at all heights as they are less inhibited by surface effects. Similar to onshore, the offshore frequency distribution also shows a high probability of lower wind speeds (between  $5\text{-}10\text{ ms}^{-1}$ ) at all heights. Higher wind speeds at lower altitudes benefits conventional WT and weakens the argument for offshore AWES as one of their benefits would be to harness energy from the stronger winds at higher altitudes. Nevertheless, also AWES benefit from these higher wind speeds. Additional reasons for placing AWES offshore are safety and land use regulations and potential cost  
 160 benefits of smaller support structure. If AWES can reliably operate autonomously they might still provide a cheaper source of electricity than conventional WT, due to their reduced material cost. Atmospheric stability of the boundary layer, which highly affects the wind speed profile shape, is commonly characterized using the Obukhov length  $\mathcal{L}$  (Obukhov, 1971; Sempreviva and Gryning, 1996). Here the application is extended to mid-altitudes.  $\mathcal{L}$  is defined by the simulated friction velocity  $u_*$ , virtual

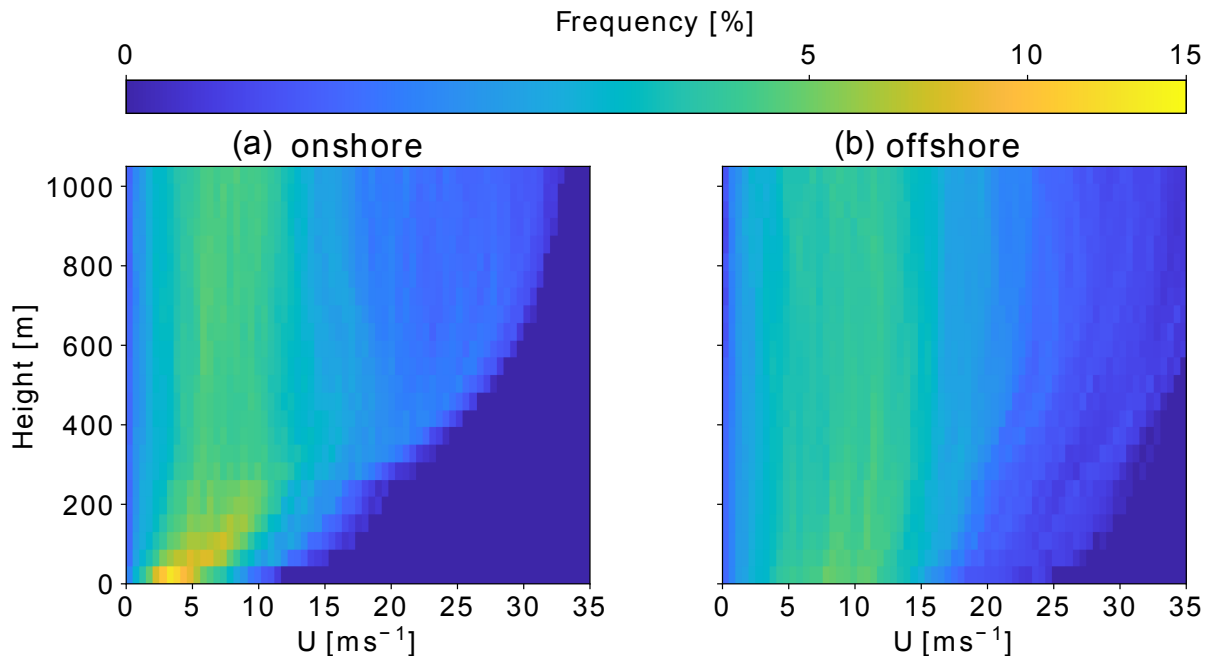


**Figure 3.** Comparison of WRF-simulated annual wind speed probability distribution at each height level between Pritzwalk (onshore left) and FINO3 (offshore right) up to 1000 m. A nonlinear color scheme was chosen to represent the high probability of low altitude onshore winds while still differentiating the lower, wide spread frequencies at higher altitudes.

165 potential temperature  $\theta_v$ , potential temperature  $\theta$ , kinematic virtual sensible surface heat flux  $Q_S$ , kinematic virtual latent heat flux  $Q_L$ , the von Kármán constant  $k$  and gravitational acceleration  $g$ :

$$\mathcal{L} = \left( \frac{-u_*^3 \theta_v}{kg} \right) \left( \frac{1}{Q_S} + \frac{0.61}{Q_L \theta} \right). \quad (1)$$

Various stability classifications using Obukhov length are defined for different wind energy sites. Table 2 summarizes the Obukhov length bin widths (Floors et al., 2011) and the frequency of occurrence of each stability class onshore and offshore, consistent with (Sommerfeld et al., 2019b).

170 Neutral stratification occurs approximately 20% of the year at both locations. The lower heat capacity of the land surface leads to a faster heat transfer and a quicker surface cool-off which favors the development of stable stratification ( $\approx 17\%$  onshore vs  $\approx 6\%$  offshore). The offshore location has a higher probability of unstable conditions which is likely caused by a warmer ocean surface compared to the air above (Archer et al., 2016).

175 Both unstable and stable conditions can lead to non-logarithmic and non-monotonic wind speed profiles. Unstable conditions are often accompanied by almost uniform wind speed profiles due to increased mixing, whereas low level jets (LLJs) can develop during the nocturnal stable onshore boundary layer (Banta, 2008). Both locations have a high chance of unassigned “other” conditions which are mostly associated with low wind speeds.



**Table 2.** Stability classes based on Obukhov lengths (Floors et al., 2011) and associated annual probability at Pritzwalk (onshore; 01.09.2015 - 31.08.2016) and FINO3 (offshore; 30.08.2013 - 14.10.2014), based on WRF results.

Stability class	$\mathcal{L}$ [m]	onshore	offshore
Unstable (U)	$-200 \leq \mathcal{L} \leq -100$	7.27%	13.66%
Nearly unstable (NU)	$-500 \leq \mathcal{L} \leq -200$	7.09%	16.34%
Neutral (N)	$ \mathcal{L}  \geq 500$	20.71%	22.82%
Nearly stable (NS)	$200 \leq \mathcal{L} \leq 500$	12.56%	5.15%
Stable (S)	$50 \leq \mathcal{L} \leq 200$	17.24%	6.20%
Very stable (VS)	$10 \leq \mathcal{L} \leq 50$	10.04%	2.96%
Other	$-100 \leq \mathcal{L} \leq 10$	25.09%	32.87%

### 3 Clustering of wind conditions

The power output of AWES highly depends on the wind velocity and its variation with height. Many temporal and spatial averages, correlations and approximations are used to describe the constantly varying wind conditions and their affect on wind energy converters. Instead of reverting to simple approximations such as the logarithmic wind speed profile, representative, WRF-simulated wind velocity profiles are chosen to compare AWES performance as realistically as possible.

Onshore (Pritzwalk) and offshore (FINO3) data are classified into groups to determine representative profiles. An accepted methodology to describe the near-surface atmosphere is atmospheric stability, commonly quantified by Obukhov length (Obukhov, 1971; Sempreviva and Gryning, 1996) which exclusively uses surface data (Section 2.2 and Equation (1)). Previous studies (Sommerfeld et al., 2019a, b) showed that Obukhov-length-classified wind speed profiles diverge with height, especially during neutral and stable conditions, which indicates vertically heterogeneous atmospheric stability and suggests that surface-based stability categorization is insufficient for higher altitudes. Clustering wind velocity profiles based on their similarity was shown result in more cohesive profile groups (Schelbergen et al., 2020b) (Figures A1 and A2). In contrast to classifying the wind regime by atmospheric stability, which requires temperature and heat flux data, clustering only uses wind data at multiple heights and groups profiles by similarity. Therefore, clustering can also be applied to wind-only measurements such as LiDAR.

The k-means clustering algorithm (Pedregosa et al., 2011) used in this study was chosen for its ease of use and scalability, due to the high dimensionality of the data set. Many other algorithms produce similar results, but a comparison between clustering algorithms is beyond the scope of this research.

Before clustering, the two horizontal wind velocity components  $u$  and  $v$ , whose vertical variation define the wind velocity profile, are rotated such that the main wind component (average wind direction up to 500 m)  $u_{\text{main}}$  points in the positive  $x$  direction and the deviation  $u_{\text{deviation}}$  is perpendicular to it, pointing in the positive  $y$  direction. This removes the directional dependency of the wind velocity profiles and results in more homogeneous clusters and simplifies the comparison of wind data

200 and `awebox` results. It is analogous to assuming omnidirectional operation. The AWES still needs to adjust to changes in wind conditions with height.

The algorithm assigns each data point, in our case wind velocity profile up to 1000 m, which comprises approximately 30 heights and 2 directions, to one of  $k$  clusters represented by their respective cluster mean (also referred to as centroid). These centroids are arranged such that they minimize the sum of the Euclidean distances (also referred to as “inertia” or “within-  
205 cluster sum-of-squares”), i.e. the cost function of the algorithm, to every data point within each cluster. As such, the centroids are usually not actual data points, but rather the average of that cluster, and will at best coincide with a data point by chance. The cluster label number is random and does not have any mathematical meaning.

The variable  $k$  refers to the fixed, predefined number of clusters. The choice of  $k$  significantly affects the accuracy of the wind resource description, the resulting power and AEP predictions (Section 6.4) as well as the computational cost associated with  
210 clustering (pre-processing) and AWES trajectory optimization (processing). The elbow method and silhouette score indicate preferable choices of  $k$ . The elbow method (Sub-Figure a in Figure 4) compares the inertia trends as a function of  $k$ .

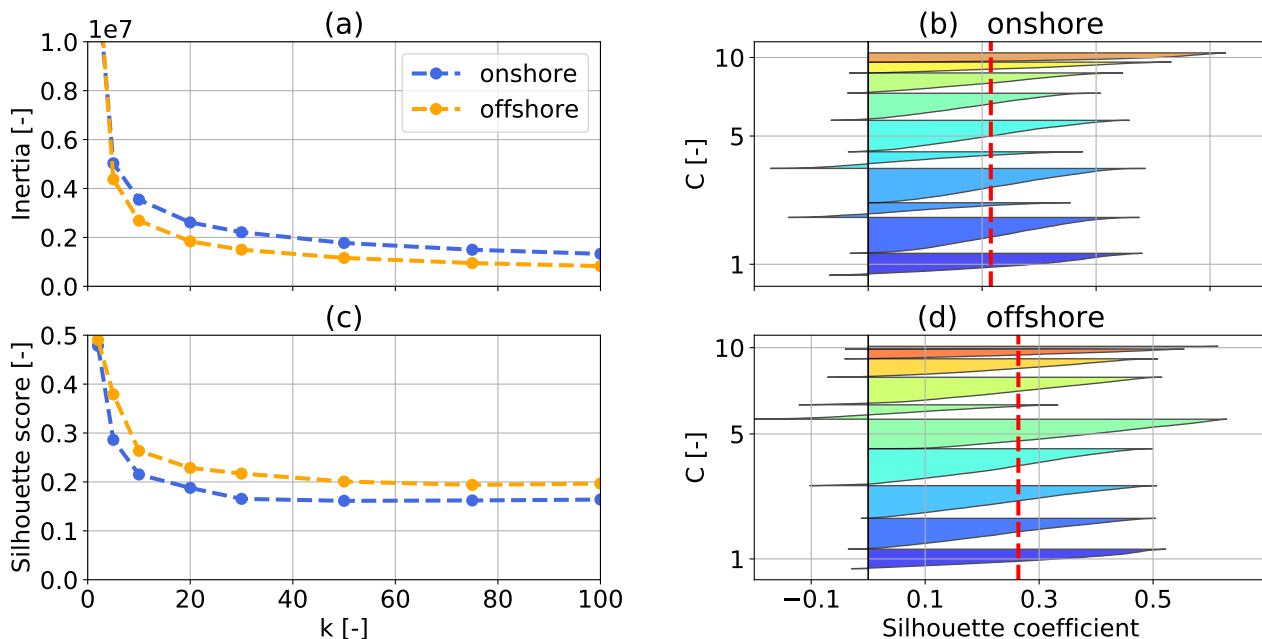


**Figure 4.**  $k$ -means clustering inertia over number of cluster  $k$  (a) for one year of onshore (blue) and offshore (orange) wind velocity profiles up to 1000 m. Silhouette score (c), average silhouette coefficients, over number number of cluster  $k$  for both locations. Onshore (b) and offshore (d) silhouette coefficients ( $k=10$ ) express the distance to neighbouring clusters. The red dashed line represents the silhouette score.

The parameter  $k$  is often chosen at a point where the inertia reduction becomes marginally small or decreases in a linear fashion with increasing number of clusters, often represented by a sharp bend or elbow in the inertia trend. A  $k$  of 20 seems to be a decent choice for the available data sets as inertia only decreases moderately for higher number of clusters which does

215 not justify the additional computational cost. Absolute values of inertia are not a normalized metric and therefore scales with  
size of the considered data set. The silhouette coefficients on the other hand are normalized between -1 (worst) and 1 (best)  
and indicate the membership of a data point to its cluster in comparison to other clusters, i.e. proximity of each data point in  
one cluster to data points in neighboring clusters. A negative value suggests that a data point is assigned to the wrong cluster.  
The silhouette score (c Figure 4) is the average of all silhouette coefficients for a fixed number of clusters  $k$ . Onshore (b) and  
220 offshore (d) silhouette coefficients for a representative  $k$  of 10. Each cluster is sorted by average wind speed up to 500 m and  
colored corresponding to the cluster centroids shown in Figure 5. Silhouette coefficients (b,d) and the resulting silhouette score  
(c) indicate good cluster coherence at both locations. The impact of number of clusters on AEP is later discussed in Sub-section  
6.4.

### 3.1 Analysis of clustered profiles

225 For visualization purposes, the following sub-sections describe the wind conditions at both locations using only  $k=10$  clusters,  
instead of the  $k=20$  clusters chosen to analyze AWES performance in Section 6. Sub-Figures a and b in Figure 5 shows the  
average wind speed profiles of the clustered wind velocity profiles, also referred to as centroids. The magnitude of the WRF-  
simulated wind velocity profiles that define their respective cluster are depicted in grey. Within a cluster, the wind speed profiles  
span a fairly narrow range of wind speeds except for a few outliers (Figures A1, A2), indicating coherent clusters. Clusters are  
230 sorted by average centroid speed up to 500 m, represented by their colors and labels ( $C = 1 - 10$ ).

As expected offshore (right) low altitude wind speeds are higher and wind shear is lower than onshore (left). Overall, offshore  
centroids are wider spread in comparison to the onshore profiles. The associated annual centroid frequency of occurrence for  
 $k=10$  is shown below in Figure 5. Wind speeds of the first and sixth offshore centroid decrease at higher altitude which could be  
caused by local or large-scale weather phenomenon. Both these clusters have a comparatively low probability. The first three  
235 onshore and offshore clusters exhibit very low wind shear with almost constant wind speed above 200 m. Onshore cluster 5,  
which seems to comprise of non-monotonic profiles as its centroid has a distinct LLJ nose at about 200 m, occurs about 5% of  
the time. Onshore centroids 7 and 8 also show a slight wind shear inversion at higher altitudes.

Evidently, the wind speed magnitude plays a dominant role in clustering as the resulting centroids are nearly ordered in  
terms of speed, especially offshore. This can lead to profiles whose shape significantly differs from the one of the centroid  
240 to be assigned to a cluster due to similar average wind speed. A clearer wind profile shape distinction could be achieved by  
normalizing the data before clustering it (Molina-García et al., 2019; Schelbergen et al., 2020a). Normalization was deferred  
to simplify and clarify the clustering procedure as the focus of this manuscript is on the derivation and comparison of AWES  
power curves. With this application in mind, it is important to note that low speed profiles with an almost constant speed up to  
high altitudes add up to about 20-30 % of annual probability. This fact is often averaged out when only long term average wind  
245 speed profile shapes are considered and can lead to an overestimation of wind speeds at higher altitudes. AWES therefore need  
to be able to either operate under such low speed conditions or be able to safely land and take-off.

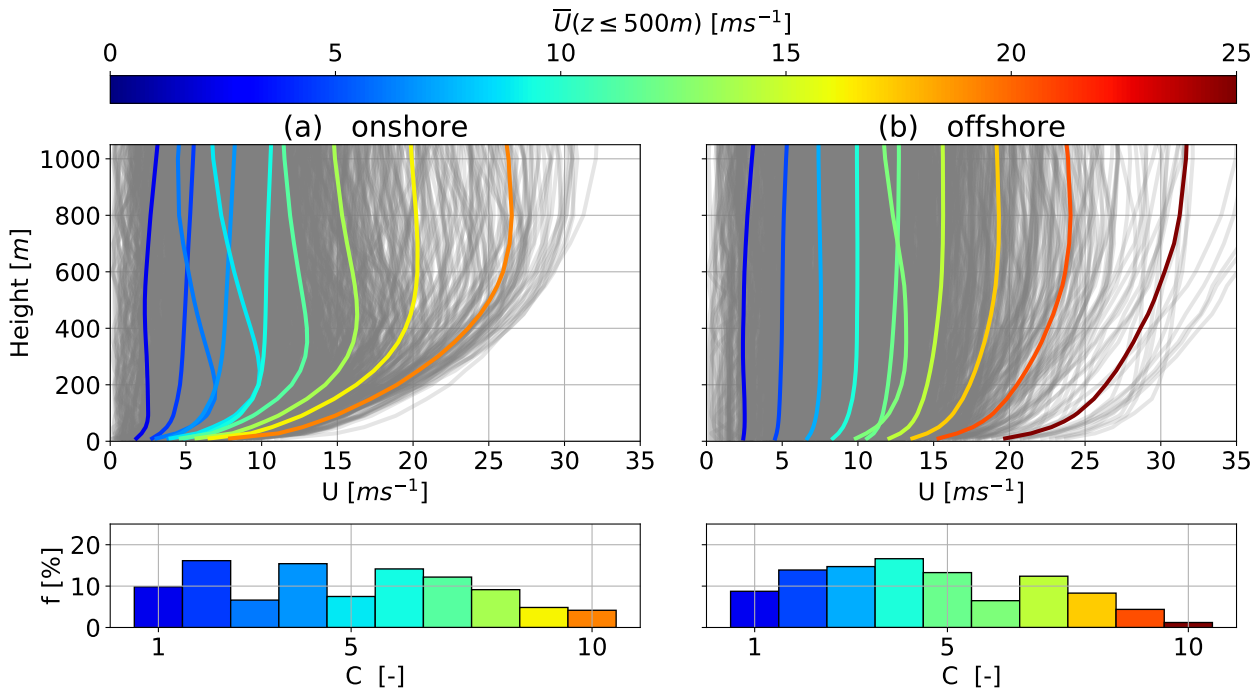


**Figure 5.** Onshore (left) and offshore (right) average annual wind speed profiles (or centroids) resulting from the k-means clustering process for  $k = 10$  over height (top). Comprising WRF simulated wind velocity profiles depicted in grey. Centroids are sorted, labeled and colored in ascending order of average wind speed up to 500 m. The corresponding cluster frequency  $f$  for each cluster  $C$  is shown below.

### 3.2 Analysis of clustered statistics

Figures 6 to 8 summarize the correlation between representative clusters ( $k=10$ ) and monthly, diurnal and atmospheric stability for the onshore (top row) and offshore (bottom row) location. This reveals patterns within the data set and gives insight into the wind prevailing regime. Clusters are sorted in ascending order of centroid average wind speed up to 500 m and colored accordingly. The corresponding centroids are shown in Figure 5.

Both locations follow a distinct annual pattern ( Figure 6) during which profiles associated with high wind speeds increase during the winter months and profiles with low wind speeds are predominantly found in summer. The two onshore and offshore clusters associated with the highest wind speed are almost exclusively present during November to February.

Offshore data shows almost no diurnal variability ( Figure 7) with only a slight increase of clusters associated with lower wind speeds during daytime. Onshore clusters on the other hand are more dependent on the diurnal cycle with a higher likelihood of low speed clusters after sunrise. The frequency of onshore cluster 5, which comprises a LLJ nose ( Figure 5), drops to almost zero during daytime and increases during nighttime, substantiating the assumption that this cluster is associated with nocturnal LLJs.

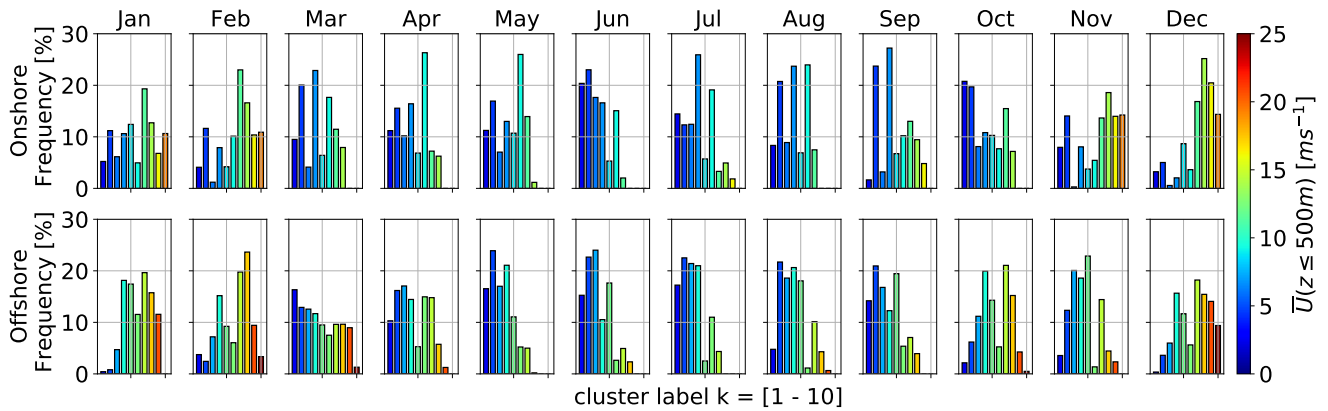


**Figure 6.** Monthly frequency of k-means clustered onshore (top) and (offshore) wind velocity profiles for a representative  $k=10$ . Clusters are sorted and colored by average wind speed up to 500 m. Centroids associated with each cluster can be found in Figure 5.

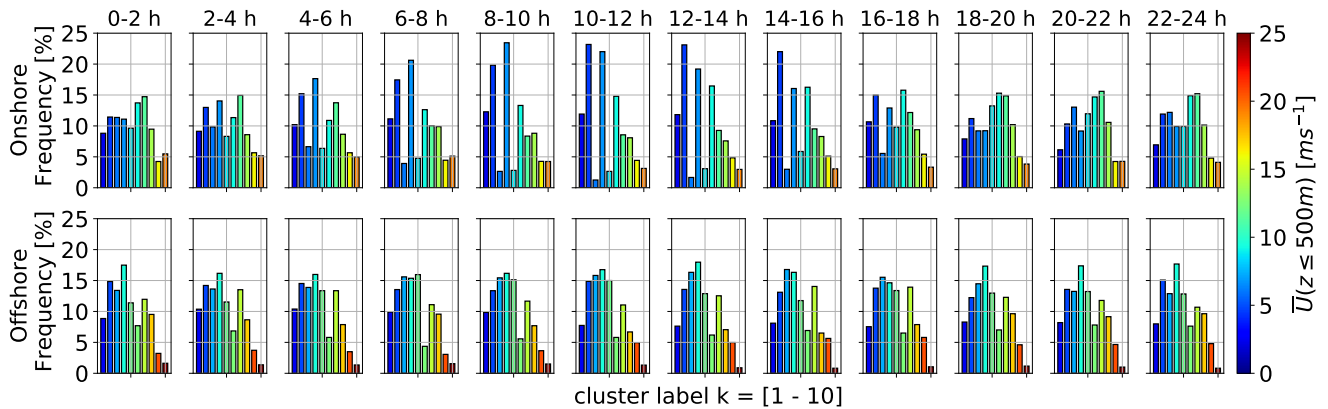


**Figure 7.** Diurnal frequency of k-means clustered onshore (top) and (offshore) wind velocity profiles for a representative  $k=10$ . Clusters are sorted and colored by average wind speed up to 500 m. Centroids associated with each cluster can be found in Figure 5.

260 The clustered wind velocity profiles and their associated speed and shape correlate with atmospheric stability as expected (Figure 8). Low wind speed clusters make up about 20% to 30% of the annual wind resource. These clusters exhibit Obukhov lengths close to zero (likely caused by very low friction velocity  $u_*$ ) and are classified as “other” because they do not fall within one of the other atmospheric stability classes according to (Floors et al., 2011) (Table2). Unstable (U) and near unstable (NU) conditions are associated slightly higher wind speeds than “other” at both locations. The highest wind speeds develop  
 265 during neutral (N) and near stable (NS) conditions. It should needs to be acknowledged that strong winds driven by large pressure gradients tend to drive the stratification towards neutral. LLJ profiles associated with onshore cluster 5 are most likely to develop during stable (S) and very stable (VS) conditions.

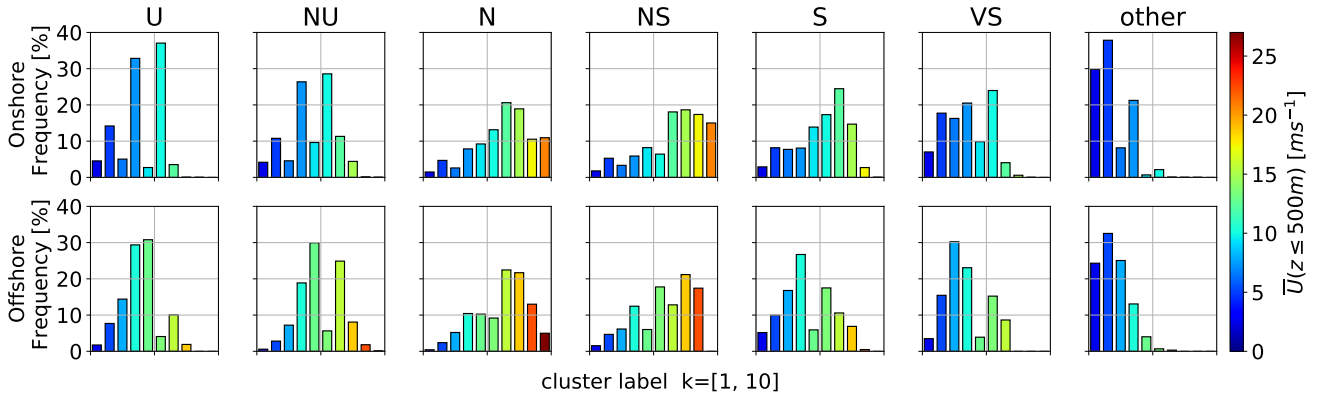


**Figure 8.** Atmospheric stability (U: unstable, NU: nearly unstable, N: neutral, NS: nearly stable, S: stable, VS: very stable) distribution of k-means clustered onshore (top) and (offshore) wind velocity profiles for a representative  $k=10$ . The associated stability classes are based on Obukhov length (Table 2). Clusters are sorted and colored by average wind speed up to 500 m. Centroids associated with each cluster can be found in Figure 5.

In conclusion, k-means clustering is able to capture and reveal temporal variations in the wind regime as well as location specific wind profile shapes up to high altitudes. Wind speed magnitude seems to determine the resulting clusters more than profile shape. Nonetheless, less common, non-monotonic profile shapes, for example profiles with LLJs, were identified. Normalizing the profiles before clustering will give more insight into the different vertical profile shapes. The corresponding cluster frequency follows the expected temporal trend and atmospheric stability association.

## 4 Dynamic AWES model

This section introduces the dynamic AWES models used in the `awebox` trajectory optimization framework (Leuthold et al., 2020) (Section 5.1). The AWES model comprises of an aerodynamic model (Sub-section 4.2), an aircraft mass model (Sub-section 4.3), a rigid tether (Sub-section 4.1) and a ground station model (Sub-section 4.4).

### 4.1 AWES model configuration

We consider a 6 degree of freedom (DOF) rigid-wing aircraft model which is connected to the ground via a rigid tether, thereby reducing the DOF to 5. It uses precomputed quadratic approximations of the aerodynamic coefficients which are controlled via aileron, elevator and rudder deflection rates (Malz et al., 2019). The tether is controlled by the tether jerk  $\ddot{l}_{\text{tether}}$  from which tether acceleration  $\dot{l}_{\text{tether}}$ , speed  $l_{\text{tether}} = v_{\text{tether}}$  and length ( $l_{\text{tether}}$ ) are integrated. The tether is modeled as a single solid rod which can not be subjected to compressive forces (De Schutter et al., 2019). The rod is divided into  $n_{\text{aero}} = 10$  elements and tether drag is calculated individually for each element relative to apparent wind speed (Bronnenmeyer, 2018), with a tether drag coefficient of  $c_D^{\text{tether}} = 1$ . The tether drag of every tether elements is equally divided between the two endpoints and finally

285 transferred to either the aircraft or ground station. This leads to an underestimation of total tether drag at the aircraft (Leuthold et al., 2018).

## 4.2 Aerodynamic model

The presented model utilizes the Ampyx AP2 from (Leuthold et al., 2020; Malz et al., 2019; Ampyx, 2020). Aspect ratio is kept constant at  $AR = 10$ . The total drag coefficient  $c_{D,\text{total}}$  highly depends on tether drag and therefore diameter  $d_{\text{tether}}$  and length  
 290  $l_{\text{tether}}$ , as well as the wing area  $A_{\text{wing}}$  and aerodynamic drag coefficient of the wing  $c_{D,\text{wing}}$ . We consider a straight, cylindrical tether with constant diameter and an aerodynamic tether drag coefficient  $c_{D,\text{tether}}$  of 1.0, which would be even higher for braided tethers. Assuming a uniform wind, the line integral along the tether results in a total effective drag coefficient of:

$$c_{D,\text{total}} = c_{D,\text{wing}} + \frac{1}{4} \frac{d_{\text{tether}} l_{\text{tether}}}{A_{\text{wing}}} c_{D,\text{tether}} \quad (2)$$

See (Houska and Diehl, 2007; Argatov and Silvennoinen, 2013; van der Vlugt et al., 2019) for details.

295 Figure 9 depicts the effect of tether drag on the  $A_{\text{wing}} = 20\text{m}^2$  scaled AP2 aircraft for tether lengths up to  $l_{\text{tether}} = 1000\text{m}$ . Lift (a) and pitch moment (c) are assumed to behave linearly, while changes in the drag coefficient (b) are approximated by a quadratic function. Tether drag is independent of aircraft angle of attack and therefore added to the zero-lift drag coefficient  $c_{D0}$ . Glide ratio  $c_L/c_{D,\text{total}}$  (e) and Loyd power factor  $c_R^3/c_{D,\text{total}}^2$  (Loyd, 1980) (f) not only decrease significantly with tether length, but optimal values move towards higher angle of attack. This effect will be less pronounced for larger wings due to  
 300 beneficial scaling effects.

## 4.3 Aircraft mass model

The aircraft dynamics are described by a single point mass of mass  $m$  and inertia  $J$ , with aerodynamic forces and moments applied to it. The dynamics of the tethered aircraft are highly dependent on aircraft mass  $m$  and inertia  $J$  which are derived by scaling the AP2 reference wing from  $A_{\text{wing}}^{\text{AP2}} = 3\text{ m}^2$  to  $A_{\text{wing}} = 20\text{ m}^2$ . Mass and inertia of a rigid wing aircraft scale relative  
 305 to wing span  $b$  with a mass scaling exponent  $\kappa$  (Equation (3)), based on Galileo's square-cube law.

$$m_{\text{scaled}} = m_{\text{ref}} \left( \frac{b}{b_{\text{ref}}} \right)^\kappa; \quad J_{\text{scaled}} = J_{\text{ref}} \left( \frac{b}{b_{\text{ref}}} \right)^{\kappa+2} \quad (3)$$

Pure geometric scaling corresponds to  $\kappa = 3$ , but in reality, as has been seen for conventional WTs, design and material improvements occur with scaling over time. A review of the available literature containing system mass details was conducted to identify an appropriate mass scaling factor. The results are shown in Figure 10; actual and anticipated AWES scale bounded  
 310 by  $\kappa = 2.2 - 2.6$  (grey area). Based on a curve fit to the available published sizing study data,  $\kappa = 2.4$  seems reasonable for future AWES development, but we leave a fulsome system AWES scaling study to future work. It can be assumed that lighter aircraft result in a lower cut-in wind speeds and higher power output.

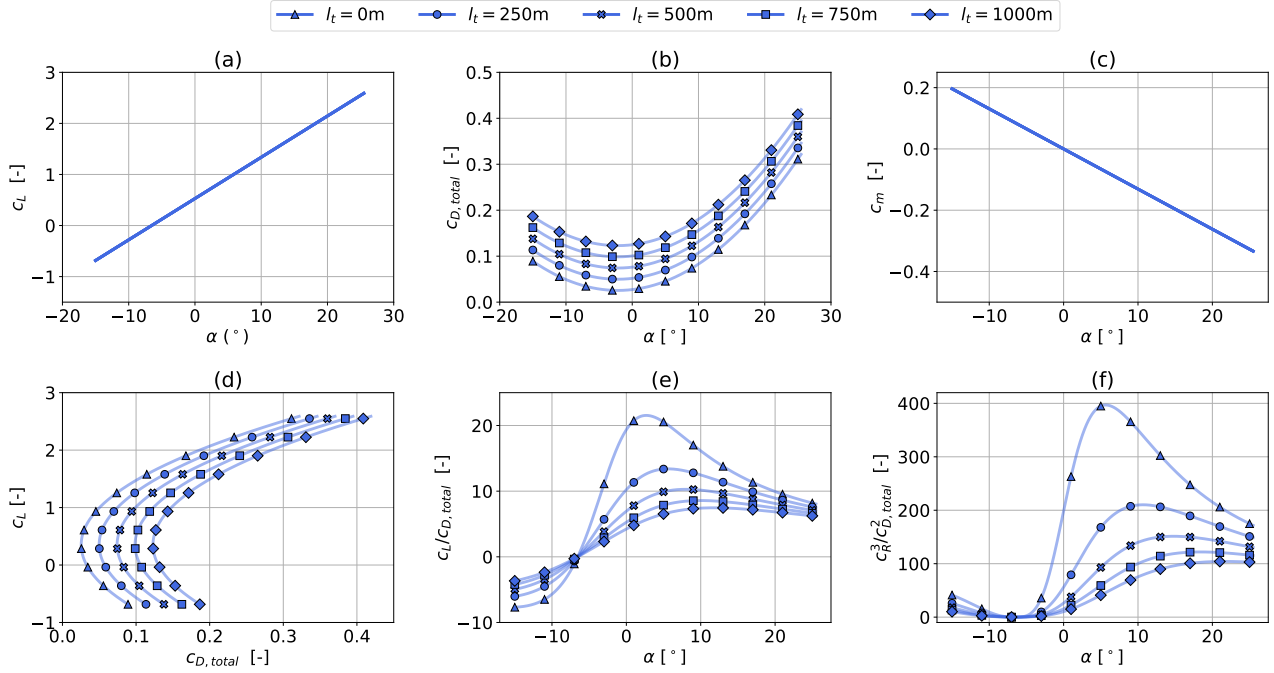


**Figure 9.** Ampyx AP2 reference wing aerodynamic lift  $c_L$  (a) and drag  $c_{D,total}$  coefficients (b) (Malz et al., 2019; Ampyx, 2020), including tether drag according to Equation (2), for a wing area  $A_{wing}$  of  $20\text{m}^2$  and tether diameter of  $D_{tether} = 7.8\text{mm}$  ( Table3. Tether length varies between 250 m and 1000 m. (c) shows the pitch moment coefficient  $c_m$  as a function of angle of attack. The bottom figures display lift over drag (d), lift to drag ratio over angle of attack (e) and  $c_R^3/c_{D,total}^2$  over angle of attack according to Loyd (Loyd, 1980).

#### 4.4 Ground station model

The ground station is not explicitly modeled in our investigation, but implemented as a set of constraints which play a decisive  
 315 role in the generated power of ground-generation AWES. Using a simplified model, optimal reel-out speed can be estimated  
 from elevation  $\theta$  and azimuth angle  $\phi$ :  $v_{out} \approx \frac{1}{3} \cos \theta \cos \phi v_{wind}$  (Section 5.5). Therefore, reel-out speed is expected to remain  
 below  $10 \text{ ms}^{-1}$  as the wind speed hardly exceeds  $20 \text{ ms}^{-1}$ . A reel-out speed of  $v_{out} = 15 \text{ ms}^{-1}$  and reel-in speed of  $v_{out} =$   
 $10 \text{ ms}^{-1}$  were chosen, resulting in a reel-out to reel-in ratio of  $\frac{2}{3}$  which is assumed to be within design limitations. A maximum  
 tether acceleration of  $\ddot{l} = 20 \text{ ms}^{-2}$  is imposed to comply with generator torque limits. The tether diameter is chosen such that  
 320 rated power is achieved at  $U_{ref} = 10 \text{ ms}^{-1}$ . Tether force constraints force tension to remain positive whilst not exceeding the  
 maximum tether stress, to which a safety factor of 3 is applied. This results in a tripling of the cross-sectional tether area. These  
 ground station and tether constraints do not represent a fully optimized AWES, but rather a representative system.



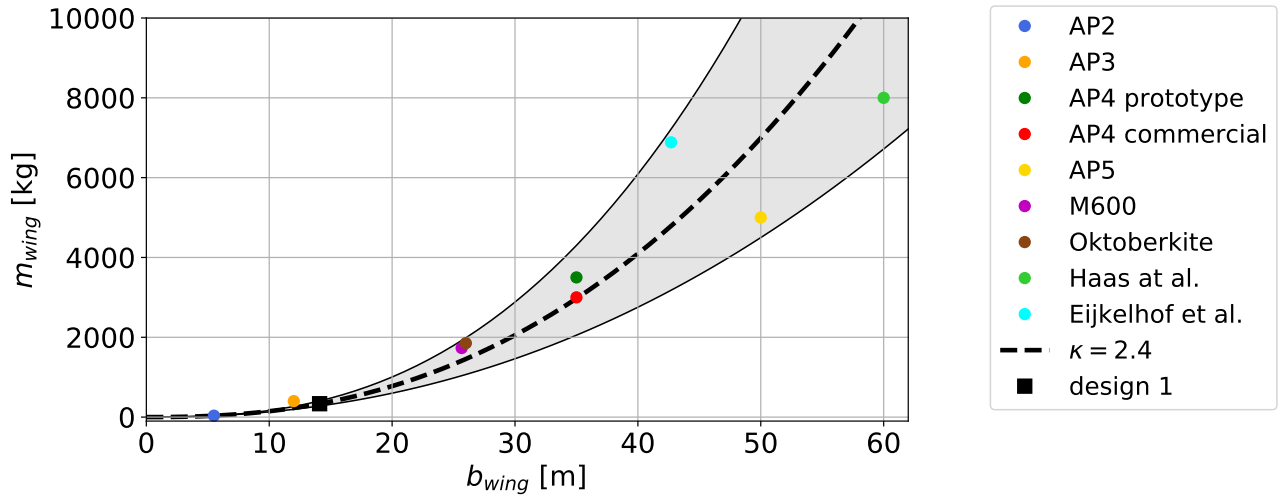


**Figure 10.** Curve fit of published sizing study AWES aircraft mass (Haas et al., 2019; Kruijff and Ruiterkamp, 2018; Eijkelhof et al., 2020; Ampyx, 2020; Echeverri et al., 2020). For these data mass scales within a scaling exponent range of  $\kappa = 2.2 - 2.6$  (grey area). The chosen mass scaling exponent of  $\kappa = 2.4$  is represented by a dashed line and the modeled design is highlighted by a black square.

## 5 Optimal control problem

Sub-section 5.1 introduces the dynamic trajectory optimization `awebbox` model (Leuthold et al., 2020). This is followed by a description of the applied constraints (Sub-section 5.2), the implementation of wind profiles (Sub-section 5.3) and solution method (Sub-section 5.4) of the optimal control problem. A simple quasi steady-state (QSS) AWES model (Sub-section 5.5) and a steady-state WT model are also introduced to compare and validate the optimization results and serve to illustrate the limitations of simplified models for performance prediction of AWES.

### 5.1 AWES model overview

AWES need to dynamically adapt to changing wind conditions to optimize power generation. This can be formulated as a trajectory optimization problem which combines the interaction between tether, flying wing and ground station. For the purposes of this study, we analyze the mechanical power produced by a single tethered aircraft and assume a straight, rigid tether. Generating dynamically feasible and power-optimal AWES flight trajectories for given wind profiles is a nontrivial task given the nonlinear and unstable system dynamics and the presence of nonlinear flight envelope constraints. Optimal control methods are a natural candidate to tackle this problem, given their inherent ability to deal with nonlinear, constrained multiple-input-multiple-output systems. In periodic optimal control, an optimization problem is solved to compute periodic system state and control trajectories that optimize a system performance index (here average AWES power output  $\bar{P}$ ) while satisfying the system dynamic equations. The initial and final state of the trajectory are freely chosen by the optimizer but must be equal to

ensure periodic operation. We here apply this methodology to generate realistic single-wing, ground-generation AWES power curves and AEP estimation based on WRF-simulated wind velocity profiles using the `awebox`. Other wind data sets, such as from a wind atlas, LiDAR campaign or met mast measurements can be implemented as well, depending on the scope and purpose of the investigation. Take-off and landing are not considered. Instead, only the production cycle, including reel-out as well as reel-in period, is optimized.

## 5.2 Constraints

The tether constraints such as tether length, speed and force are summarized in Table 3. Flight envelope constraints include limitation of aircraft acceleration, roll and pitch angle (to avoid collision with the tether) and angle of attack. The lift coefficient is assumed to be linear within this range. Furthermore, a minimal operating height of  $z_{\min} = 50 + \frac{A_{\text{wing}}}{2}$  m is imposed for safety reasons.

**Table 3.** Aircraft design parameters for AWES  $A_{\text{wing}} = 20 \text{ m}^2$  analyzed in this study and for the original AP2 aircraft. Values in square brackets represent flight envelope bounds, which are implemented as inequality constraints of the optimization.

	Parameter	AP2	design 1
Aircraft	wing area [ $\text{m}^2$ ]	3	20
	wing chord [m]	0.55	1.42
	wing span [m]	5.5	14.1
	wing AR [-]	10	10
	kite mass [kg]	36.8	355
	$\beta$ [ $^\circ$ ]		[-15 : 15]
	max. air speed [ $\text{ms}^{-1}$ ]		75
Tether	max. length [m]		2000
	speed [ $\text{ms}^{-1}$ ]		[-15 : 10]
	max. acceleration [ $\text{ms}^{-2}$ ]		[-10 : 10]
	diameter [mm]		7.8
	max. stress [Pa]		$3.6 \cdot 10^9$
	max. force [kN]		60
	min operating altitude [m]		60

## 5.3 Wind profile implementation

Representative wind velocity profiles derived from WRF, described in Section 2 and clustered in Section 3, are implemented into the trajectory optimization framework (Section 4) to determine optimal trajectories, mechanical AWES power and derive power curves. These results are references against AWES performance subject to a standard logarithmic wind speed profile. The 2D wind components are rotated such that the main wind direction ( $u_{\text{main}}$  as defined by the average wind direction up

to 500 m, compare Section 3) is in positive  $x$  direction and the deviation from it in  $y$  direction. This is equivalent to assuming  
 355 omnidirectional AWES operation with the wing still needing to adjust to changing wind conditions with height. Furthermore,  
 we include a simplified atmospheric model based on international standard atmosphere to account for air density variation.

AWES trajectories depend on prevailing wind conditions as they greatly benefit from continuously adapting their operational  
 altitude, tether speed and path to maximize power production and minimize losses. Within each cluster, three WRF-calculated  
 wind velocity profiles are chosen and implemented into the trajectory optimization framework. To that end, wind velocity  
 360 profiles are sorted based on the average wind speed up to 500 m, which is used as an a priori proxy for operating height.  
 From these sorted wind profiles, the 5th, 50th and 95th percentile profile are chosen and assumed to be representative of the  
 spectrum of wind conditions within this cluster. These three wind profiles of every cluster function as boundary conditions in  
 the dynamic optimization model (Section 5) and are used in the simplified QSS model (Sub-section 5.5). To implement the  
 wind velocity profile into the optimization framework, the  $u$  and  $v$  components of the wind velocity profile are interpolated  
 365 individually using Lagrange polynomials. Lagrangian polynomials were chosen because the function passes through the data  
 points, but any other polynomial could have been chosen as long as the derived function is twice continuously differentiable.  
 This is necessary to implement them into the optimal control problem that can be solved with the gradient-based nonlinear  
 programming (NLP) solver IPOPT (Wächter and Laird, 2016). Therefore, the analyses in Section 6 are based on three wind  
 profiles for each of the  $k=5,10,20,50$  clusters (Section 3).

370 For comparison, logarithmic wind speed profiles (Equation (4)), with a roughness length of  $z_0^{\text{onshore}} = 0.1$  and  $z_0^{\text{offshore}} =$   
 0.001, are implemented into the trajectory optimization framework.

$$U_{\log} = U_{\text{ref}} \left( \frac{\log_{10}(z/z_0)}{\log_{10}(z_{\text{ref}}/z_0)} \right) \quad (4)$$

Reference wind speed  $U_{\text{ref}}$ , at reference height  $z_{\text{ref}} = 10$  m, varies from 3 to 19  $\text{ms}^{-1}$  with a step size of  $\Delta U_{\text{ref}} = 2 \text{ms}^{-1}$ .

#### 5.4 Problem formulation and solution

375 AWES trajectory optimization is a highly nonlinear and non-convex problem which likely has multiple local optima. Therefore,  
 the particular results generated by a numerical optimization solver can only guaranty local optimality, and usually depend on  
 the chosen initialization. This can result in unwanted or unrealistic AWES trajectories, which implies that the quality of all  
 solutions needs to be evaluated a posteriori.

A periodic optimal control problem is formulated to maximize the average cycle power  $\bar{P}$  of a single AWES subject to  
 380 equality (e.g. tether diameter) and inequality constraints described above (De Schutter et al., 2019; Leuthold et al., 2018). The  
 trajectory optimization problem is discretized into 100 intervals using direct collocation.

An initial guess is generated using a homotopy technique similar to (Gros et al., 2013). A circular trajectory is estimated  
 based on a fixed number of loops (here  $n_{\text{loop}} = 5$ ) at a  $15^\circ$  elevation angle and the initial tether length. Initial aircraft speed  
 is based on the estimated duration of a single loop (here 10 sec). Previous analyses showed that the `awebox`-estimated power  
 385 output is insensitive to the number of loops and therefore flight time, at least for less than 10 loops. The homotopy technique

initially fully relaxes the dynamic constraints using fictitious forces and moments to reduce model nonlinearity and coupling, improving the convergence of Newton-type optimization techniques. The constraints are then gradually re-introduced until the relaxed problem matches the original problem. The resulting nonlinear program (NLP) is formulated in the symbolic modeling framework CasADi for Python (Andersson et al., 2019) and solved using the linear solver MA57 (HSL, 2020) in IPOPT  
 390 (Wächter and Biegler, 2006).

## 5.5 Engineering reference model

AWES power production is intrinsically linked to the aircraft's flight dynamics, as the AWES never reaches a steady state over the course of a power cycle. he employed QSS ground-generation AWES model (Equation (5)) (Schmehl et al., 2013), adapted from Loyd's crosswind power approximation (Loyd, 1980), simplifies the complex trajectory of a rigid body to a single point  
 395 mass in a state of equilibrium, pointing directly crosswind. Optimal power  $P_{\text{opt}}$  is described as a function of wind speed  $U$ , air density  $\rho_{\text{air}}$  and the resultant aerodynamic force coefficient  $c_{\text{R}}$  (Equation (6)), which is calculated from the aerodynamic lift  $c_{\text{L}}$  and total drag coefficient  $c_{\text{D,total}}$ , including wind and tether drag. The QSS model is subject to the same representative, simulated WRF wind profiles as the dynamic optimization framework.

$$P_{\text{opt}} = \frac{\rho_{\text{air}}(z)}{2} A_{\text{wing}} U^3(z) c_{\text{R}} \left( \frac{c_{\text{R}}}{c_{\text{D,total}}} \right)^2 f_{\text{opt}} (\cos \theta \cos \phi - f_{\text{opt}})^2 \quad (5)$$

$$400 \quad c_{\text{R}} = \sqrt{c_{\text{L}}^2 + c_{\text{D,total}}^2} \quad (6)$$

Under ideal conditions, this model predicts optimal instantaneous power for a given AWES design and wind conditions. For every wind speed profile maximum power is determined by varying operating height and angle of attack. We assume the AWES to produce optimal power throughout the entire reel-out phase and neglect reel-in losses, because of negligible tether tension during reel-in. Aircraft and tether mass are neglected. Tether speed  $v_{\text{t}}$  is non-dimensionalized in the form of the reeling factor  
 405 ( $f = \frac{v_{\text{t}}}{U}$ ) and assumed to take the optimal value of  $f_{\text{opt}} = \frac{1}{3} \cos \theta \cos \phi$ . The aircraft is assumed to move directly crosswind with a zero azimuth angle  $\phi = 0$  relative to the wind direction. All aerodynamic forces and the tether tension act on the single point mass and result in an equilibrium state. The elevation angle  $\theta = \arcsin(\frac{z}{l_{\text{tether}}})$  is derived from altitude  $z$  and tether length  $l_{\text{tether}}$  and describes the losses associated with the misalignment between an assumed horizontal wind direction and an inclined tether. The total drag coefficient  $c_{\text{D,total}}$  determines the aerodynamic drag of the entire AWES, comprising kite and tether, in  
 410 crosswind motion. It highly depends on the tether diameter  $d_{\text{tether}}$  and length  $l_{\text{tether}}$ , as well as the wing area  $A_{\text{wing}}$  and its aerodynamic drag coefficient  $c_{\text{D,wing}}$  defined by the wing shape. A tether diameter  $D_{\text{tether}} = 7.8\text{mm}$  is chosen such that rated wind speed is achieved at  $v_{\text{rated}} = 10\text{m.s}^{-1}$  (Table3).

Beyond rated wind speed, tether length, operating height and angle of attack are chosen to stay within the constraints (see Sub-section 5.2) which apply to both the dynamic optimization model and the QSS model.

$$415 \quad P_{WT} = c_p^{WT} \frac{1}{2} \rho_{air} A_{WT} U^3 (z_{WT} = 100 \text{ m}) \quad (7)$$

Hub height  $z_{WT}$  is assumed to be 100 m for both onshore and offshore WT. Rotor diameter  $D_{WT} \approx 35\text{m}$  and swept area of the turbine  $A_{WT} \approx 1425\text{m}^2$  is chosen such that rated power, at a rated wind speed of  $v_{rated} = 10\text{m}\cdot\text{s}^{-1}$ , is equivalent to AWES rated power  $P_{rated} = 260\text{kW}$ , assuming a constant power coefficient of  $c_p^{WT} = 0.45$ .

## 6 Results and discussion

420 This section describes AWES trajectories and time series (Sub-section 6.1) results generated by the trajectory optimization toolbox (Section 4) and compares them to a quasi-steady reference AWES model (Sub-section 5.5). Wind boundary conditions are based on simulated onshore (Pritzwalk) and offshore (FINO3) wind data (Section 2). Representative wind velocity profiles have been chosen from clustered wind data (Section 3). Sub-section 6.2 examines operating height statistics and tether length trends. Lastly, we compare AWES performance in terms of power curve (Sub-section 6.3) and annual energy production (AEP) 425 (Sub-section 6.4).

### 6.1 Flight trajectory and time series results

This sub-section offers insight into typical optimized AWES flight trajectories. Figures 11 and A3 compare the trajectories of representative onshore and offshore wind conditions between typical low and high wind speeds for an aircraft with a wing area of  $A_{wing} = 20 \text{ m}^2$ . These trajectories and wind velocity profiles have only been chosen to visualize the range of wind 430 conditions and the resulting trajectories. They do not depict special circumstances.

Figure 11 and A3 show the wind speed profiles  $U$  over altitude  $z$  (a) with the operating height highlighted in color. The colored segments also depict the Lagrange polynomials that interpolate the WRF simulation data for optimization purposes. Sub-figure c shows a top view of the wind velocity profile (rotated horizontal  $u_{main}$  and  $u_{deviation}$  wind component) in grey up to 1000 m displayed above as well as the part of the profiles corresponding to the height range swept by the aircraft in color. 435 The two center plots show the optimized trajectory in side view (b, x-z plane) and top view (d, x-y plane).

When maximum tether force is reached the system starts to de-power while maintaining the same high tension (Sub-figure e in Figures 11 and A3). Such trajectories often extend perpendicular to the main wind direction. This often results in odd or unexpected trajectories, even though these local minima are within the system constraints (roll rate etc.). De-powering by increasing the elevation angle is also possible and likely to happen, but harder to determine as it is not easily identifiable 440 whether the elevation angle increased due to better wind conditions or to de-power the wing. Reducing the angle of attack (g) while maintaining constant maximum tether force (e) can be observed in the highest onshore wind speed trajectory (green). During the production loops, the angle of attack constraint of the red and orange trajectories are active. The AWES angle of

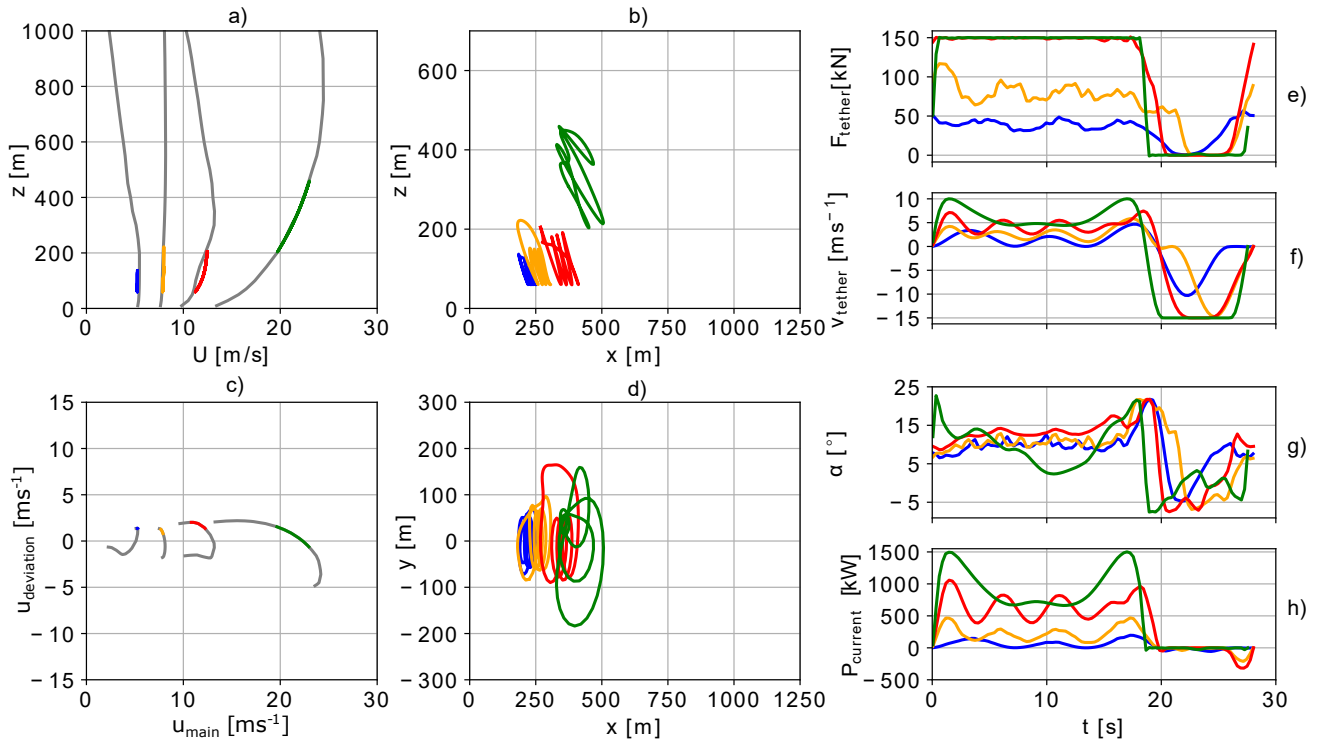


**Figure 11.** Representative wind speed profiles (a), and hodograph (top view) of wind velocity up to 1000 m (c). Wind profiles chosen to represent typical low (blue, orange), medium (red) and high wind speeds (green). Trajectories (b,d) in side and top view. Temporal variations of tether force  $F_{\text{tether}}$  (e), tether speed  $v_{\text{tether}}$  (f), angle of attack  $\alpha$  (g) and instantaneous power  $P_{\text{current}}$  (h) optimized based on clustered onshore wind speed profiles for a ground-generation AWES with a wing area of  $A_{\text{wing}} = 20 \text{ m}^2$ .

attack at the onshore location is generally higher than offshore (Sub-figure g in Figure 11 and A3). This can likely be attributed to the fact that onshore tether lengths are generally longer than offshore, where beneficial wind conditions allow the AWES to operate at lower altitudes Section 6.2. As a result, the optimal  $c_L^3/c_D^2$  shifts towards higher angle of attack.

The algorithm seems to always maximize tether force and vary tether speed (f) close to optimal reel-out speed ( $v_{\text{out}} \approx \frac{1}{3} v_{\text{wind}}$  (Loyd, 1980)) to maximize average cycle power. At high wind speeds the trajectory starts to differ from its predefined shape with distinct loops and the system de-powers, which can be seen in the power development during the production phase (green). Trajectories for such high speed wind conditions without a tether force constraint, where the tether diameter is adjusted to the wind conditions, would be closer to the looping paths seen for lower wind speeds (blue, orange, red). The optimizer tries to keep the reel-in phase as short as possible, given tether speed and acceleration constraints. As a result, the reel-in tether speed reaches its limit for high wind speeds. The time history of instantaneous power  $P_{\text{current}}$  (h) clearly distinguishes the production and consumption phase of pumping-mode (ground-generation) AWES.

All optimized trajectories have a close to zero power usage during reel-in as they reduce the angle of attack to near zero lift conditions. One commonality between all time series is that they almost all have the same flight time independent of location, wind speed or aircraft size. The flight time is almost solely determined by the initial number of loops, here five, used in the initialization procedure. This is likely a result of the optimization algorithm. The optimized trajectories result in almost zero tether force, and therefore energy consumption, during the reel-in phase. Based on previous analyses, net mechanical AWES power output seems to be insensitive to the number of loops and flight time. This might be different for real deployment, where a higher number of loops could be beneficial, because the reel-in time relative to reel-out time could be shorter.

## 6.2 Tether length, elevation angle and altitude

This sub-section compares tether lengths and operating altitudes for a wing size of  $A_{\text{wing}} = 20 \text{ m}^2$ . Data are based on 60 wind velocity profiles from  $k=20$  cluster, both onshore (Pritzwalk) and offshore (FINO3) (Sub-section 5.3). Within every cluster the p5, p50, p95-th wind profiles is chosen to represent the range of wind conditions aggregated in this cluster.

Figure 12 (a) illustrates the range of onshore (blue) and offshore (orange) AWES tether length  $l_{\text{tether}}$  of each wind velocity profile. The maximum is and minimum, highlighted by a square, are plotted over reference wind speed  $U(z_{\text{ref}} = 100-400 \text{ m})$ . Neither of the optimizations reaches the maximum tether length of  $l_{\text{tether}}^{\text{max}} = 2000 \text{ m}$ . Both locations show a trend towards longer tether lengths until rated wind speed. Beyond rated wind speed, tether lengths stay constant or even decrease as the system de-powers and tries to stay within constraints. The slightly lower tether length offshore is probably due to lower wind shear and more homogeneous wind regime (Sub-section 2.2). The onshore data set displays multiple outliers, probably due to wind velocity profile variation, further supporting the need to dynamically adapt AWES operating conditions.

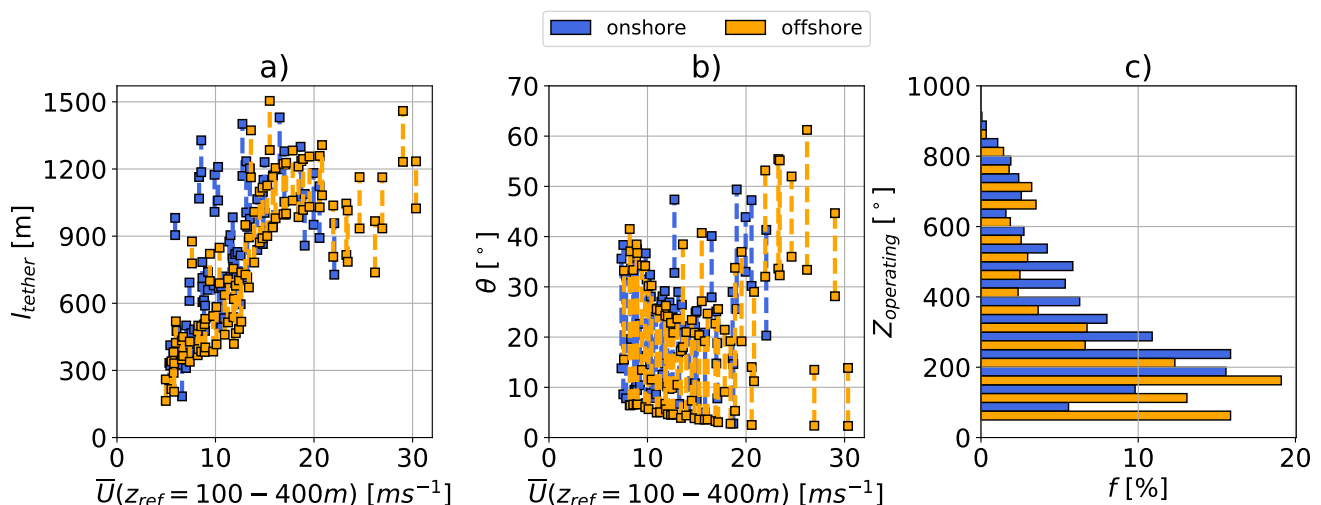


**Figure 12.** Tether length range (a) over reference wind speed  $U(z_{\text{ref}} = 100 - 400 \text{ m})$  and frequency distribution of operating altitude (b) based on `awebox` trajectory optimization of  $k=20$  onshore (blue) and offshore (orange) clusters.

Sub-figure (c) shows the elevation angle  $\theta$  as a function of reference wind speed  $U(z_{\text{ref}} = 100 - 400\text{m})$ . As expected, the optimizer tries to keep elevation angle low to reduce misalignment losses. However, the tether length increase with wind speed leads to an overall increase in operating heights. Both onshore and offshore follow a similar trend.

475 The right side of the Figure 12 (c) shows the frequency distribution of operating altitude  $z_{\text{operating}}$ , calculated from the trajectory described in Sub-section 6.1. Operating altitudes over the entire wind regime, both off- and onshore, are almost never higher than 500 m above ground, confirming findings in (Sommerfeld et al., 2019a, b). Optimal operating heights at both locations is below 400 m for almost 78 % of the year. Larger or Multi-wing AWES could benefit from higher operating altitudes due to their higher lift to tether drag ratio and weight ratio, but more detailed analyses are required.

### 480 6.3 Power curve

This subsection compares power curves derived from power-optimal trajectories, subject to clustered WRF profiles or logarithmic profiles (Sub-section 5.3), to QSS modeled power as well as a WT reference. Furthermore, the impact of different reference heights on AWES power curves, wind speed probability and annual energy distribution is illustrated.

Figure 13 (a, b) shows optimized AWES power based on onshore (blue) and offshore (orange)  $k=20$  clustered WRF profiles  
 485 (data points), with a least square fit (dashed line). Optimized AWES power based on logarithmic wind speeds (Equation (4)) with a roughness lengths of  $z_0^{\text{onshore}} = 0.1$  and  $z_0^{\text{offshore}} = 0.001$  (Sub-section 5.3) are depicted as dotted lines. These data are compared to AWES QSS model (solid line) as well as a simplified WT model (red line) described in Sub-section 5.5, both of which use the same clustered WRF wind velocity profiles as the dynamic optimization model. The cut-in wind speed of  $5\text{ m}^{-1}$  is the result of unconverged optimizations below this threshold. No cut-out wind speed was defined. Therefore, energy  
 490 conversion is only limited by the wind resource. The presented AWES and WT reach rated power around  $U_{\text{rated}} \approx 12\text{ms}^{-1}$ . To simplify the readability and applicability of the methodology, as well as to be consistent with the power curve definition of conventional wind turbine, a single reference wind speed is chosen to represent the complex wind conditions. We chose average wind speed between 100 and 400 m as reference wind speed (abscissa) because the optimized AWES trajectories mostly operate in this height range (Sub-section 6.2). The shape of the power curve changes depending on reference height  
 495 which further illustrates the importance of standard AWES reference wind conditions. For the calculation of WT wind speed and energy distribution a reference height of 100 m is used. The clustered power curve fit aligns well with optimization results for logarithmic wind speed profiles at this reference height.

The power harvesting factor (Equation (8)) (Diehl, 2013), shown in sub-figures c and d, expresses the estimated AWES power  $P$  relative to the total wind power through an area the same size as the wing  $P_{\text{area}}$ .

$$500 \quad \zeta = \frac{P}{P_{\text{area}}} = \frac{P}{\frac{1}{2}\rho_{\text{air}}A_{\text{wing}}U(z)^3} \leq \frac{4}{27}c_{\text{R}} \left( \frac{c_{\text{R}}}{c_{\text{D}}} \right)^2 \quad (8)$$

$\zeta$  is calculated with the average wind speed between  $U_{\text{ref}}(z = 100\text{m} - 400\text{m})$  as a proxy for operating heights. At low wind speeds the optimization model finds higher power output than the QSS model. This is likely caused by the choice of reference wind speed which leads to a shift in these data points towards lower wind speeds.



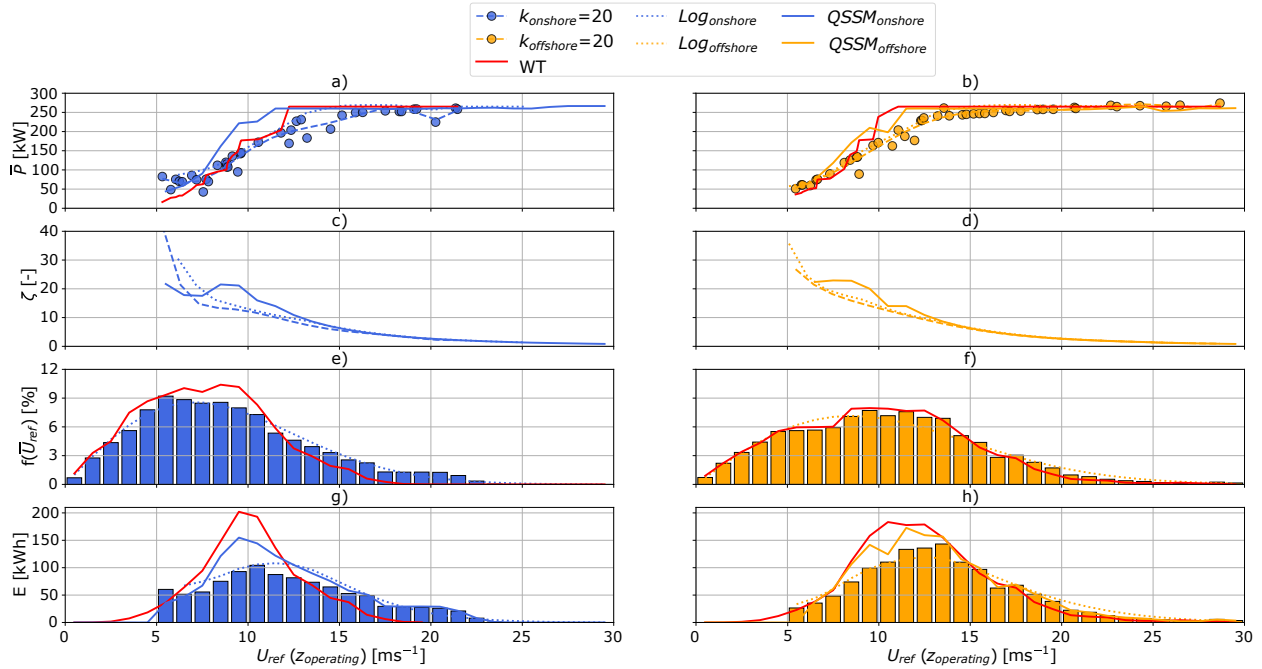


**Figure 13.** Onshore (blue) and offshore (orange) AWES power curves (a,b) over average wind speed at operating height based on 3 wind profiles for each of the  $k=20$  clusters. Simplified WT model (red lines), QSS AWES model (solid lines) and AWES subject to logarithmic wind boundary conditions (dotted lines) with rated wind speed of  $v_{rated} = 10\text{ms}^{-1}$  and the same rated power for reference. Harvesting factor  $\zeta$  (Equation (8)) shown in c, d. Annual energy distribution (e,f) based on power curves and WRF-simulated annual wind speed probability distributions (c,d) and standard Rayleigh distributions. (International Electrotechnical Commission, 2010).

Sub-figures e and f show the wind speed probability distribution for the chosen average reference wind speeds between 100 and 400 m (bars), at 100 m WT hub-height (red line) and the standard Rayleigh distribution (dotted lines) with  $U_{onshore}^{ave} = 10\text{ms}^{-1}$  and  $U_{offshore}^{ave} = 12\text{ms}^{-1}$  (Equation (11)) (International Electrotechnical Commission, 2010). As expected, higher operating altitudes reach higher wind speeds. However, low wind speeds of less than  $5\text{ms}^{-1}$  still occur almost at the same frequency as at lower altitude, both onshore and offshore.

These distributions, together with the power curves, are used to generate the annual energy distribution in sub-figures g and h. In comparison to conventional WT, the AWES energy distribution is shifted towards higher wind speeds. For AWES to convert power during these conditions, the flight path needs to be adjusted to de-power so that the AWES stays within material strength limitations.

In contrast to conventional WT with their fixed hub-height, AWES adapt their operating heights dynamically, which makes the choice of reference wind speed non-trivial. Due to many conceptually different AWES designs and the novelty of the technology, no generally accepted AWES power curve definition exists. Similarly, no standard wind resource model such as

the Rayleigh or Weibull distribution for conventional wind has been defined. Figure 14 investigates the impact of different reference heights on AWES power curve representations (a,b)

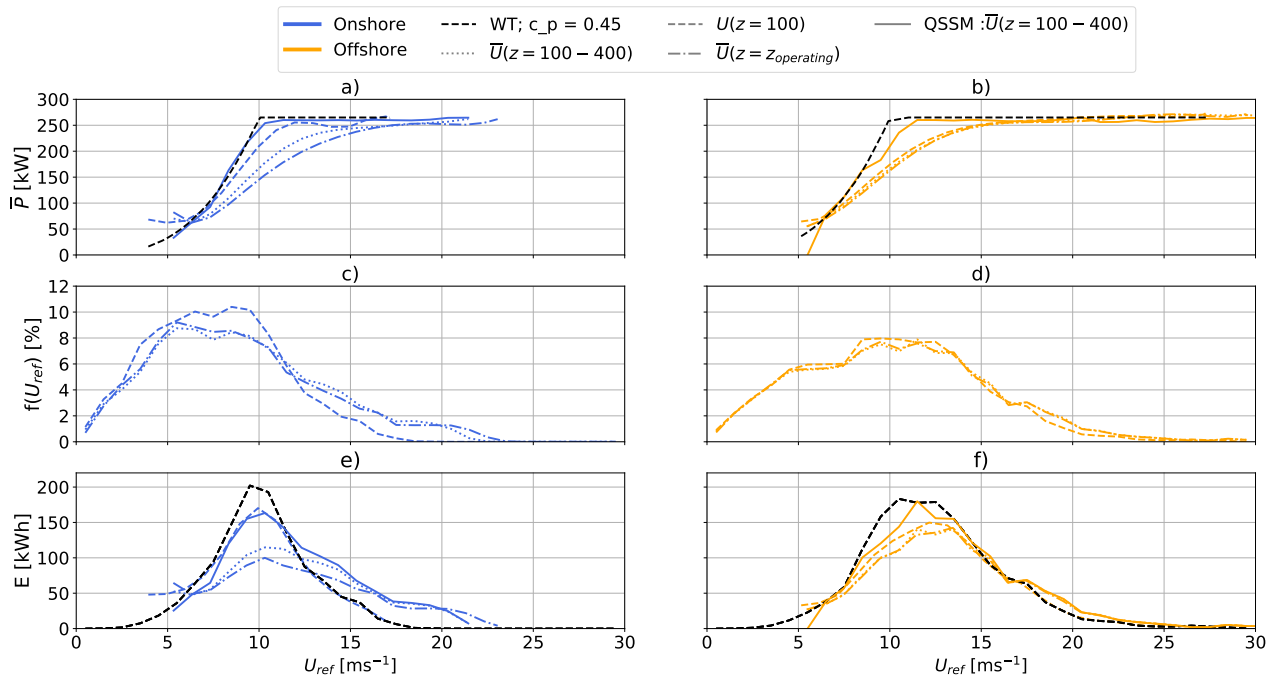


**Figure 14.** Onshore (blue) and offshore (orange) AWES power curves (a,b) over various reference wind speeds (dashed lines: fixed height  $z = 100$  m; dotted lines:  $z = 100 - 400$  m; dash-dotted lines: average wind speed along operating trajectory) based on 3 wind profiles for each of the  $k=20$  clusters. A simplified WT (dashed black lines) and QSS AWES model (solid line) with same rated power are depicted as reference. Power curves and WRF-simulated annual wind speed probability distribution (c,d) for various reference heights result in annual energy production distribution (e,f) and AEP estimates.

These power curves are derived from curve fits of 3 wind velocity profiles within each of the  $k=20$  onshore (blue) and offshore (orange) clusters. Together with differing wind speed probability distributions (c,d) this leads to varying annual energy production (AEP) further analyzed in Sub-section 6.4. The area underneath the distribution accumulates to the annual energy production (AEP) further analyzed in Sub-section 6.4. WT data with a reference wind speed at  $z = 100$ m (black dashed lines) and QSS data with an average reference wind speed between  $100 \leq z \leq 400$ m (solid lines) are included for comparison.

The presented AWES and WT start producing significant power around  $U \approx 5 \text{ ms}^{-1}$  and reach rated power between 12 and  $15 \text{ ms}^{-1}$  at their respective reference heights. Whereas the onshore AWES power curve with a fixed reference height of 100 m almost aligns with the power curve of a conventional wind turbine, other power curves are seemingly below that. This is likely caused by higher wind shear and non-monotonic wind speed profiles which lead to faster winds aloft and higher operating altitudes with lower wind speeds at 100 m. For monotonically increasing wind speeds this leads to data points moving to the right when plotted against  $u_{100-400m}$  in comparison to when they are plotted against  $u_{100m}$ . Offshore winds

however experience less shear (Sub-section 2.2), which is why offshore AWES power curves for any reference height almost  
 530 overlap with each other. AWES energy production distribution is shifted towards higher wind speeds, particularly onshore, due  
 to higher average wind speeds at operating height. Furthermore, the distribution of AWES energy production shows a wider  
 spread as the system operates within a wider range of wind speeds.

#### 6.4 Annual Energy Production

Long-term wind statistics are necessary to determine reliable Annual Energy Production. Wind resource assessment guidelines  
 535 typically recommend multi-year wind measurements and long-term wind data corrections via simulations. We only consider  
 wind data for the simulated one-year time span (Section 2) to simplify the analyses in this research. AEP (Equation 9) is  
 approximated by the sum of the annual energy distribution shown in Figures 13 and 14, which is the multiplication of cycle-  
 average power  $\bar{P}$  and wind speed probability  $f(\bar{U}_{\text{ref}})$ , binned into  $n_{\text{bin}}$  bins with  $\Delta U_{\text{bin}} = 1\text{ms}^{-1}$ .

$$AEP = \sum_{i=1}^{n_{\text{bin}}} (\bar{P}_i \cdot f(\bar{U}_{\text{ref}})_i) \quad (9)$$

Figure 15 compares several AEP estimations of optimized AWES trajectories based on WRF data as well as logarithmic  
 wind profiles ( $AWES_{\text{log}}$ ). These results are referenced against AEP predictions using the QSS AWES model ( $QSS(100\text{m} \leq$   
 $z \leq 400\text{m})$ ) and steady-state WT model ( $WT(z = 100\text{m})$ ). We compare the impact of reference height on AEP, since no  
 standard reference height is defined for AWES wind statistics. WRF-based AEP estimates use the wind statistics derived from  
 the one-year WRF simulation at  $z=100\text{m}$ , average wind statistics between  $100\text{m} \leq z \leq 400\text{m}$  or average wind statistics along  
 545 the flight path  $z_{\text{operating}}$ . These are compared to AEP assessed from the summation of power (Equation (10)) over every  $n$   
 10-min wind speed profile during the one year simulation ( $AWES_{\text{cluster}}$ ). For this approach, power  $P_{i,j}^{\text{interp}}$  is interpolated  
 between p5, p50 and p95 within each cluster  $k$  and then added up to an annual total energy. The profiles within each cluster  
 are sorted by wind speed up to 500 m, which is used as an a priori proxy for operating height (5.3). We assume that the  
 cycle-average power represents the average power for this time period.

$$AEP = \sum_{j=1}^k \sum_{i=1}^n (P_{i,j}^{\text{interp}}) \quad (10)$$

In the case of the previously described logarithmic wind speed profiles, a standard Rayleigh distribution (Equation (11))  
 (International Electrotechnical Commission, 2010) with  $U_{\text{onshore}}^{\text{avg}} = 10\text{ms}^{-1}$  and  $U_{\text{offshore}}^{\text{avg}} = 12\text{ms}^{-1}$  at  $z = 100\text{m}$  is used to  
 estimate AEP ( $AWES_{\text{log}}$ ).

$$f_{\text{Rayleigh}} = \frac{2U}{U_{\text{avg}}} \exp - \left( \frac{U}{U_{\text{avg}}} \right)^2 \quad (11)$$

555 Both onshore (blue) and offshore (orange) AEP vary with number of clusters. However, AEP variation is negligible for more  
 than  $k=20$  and the possible improvement in energy prediction does not justify the increased computational cost. Less wind shear

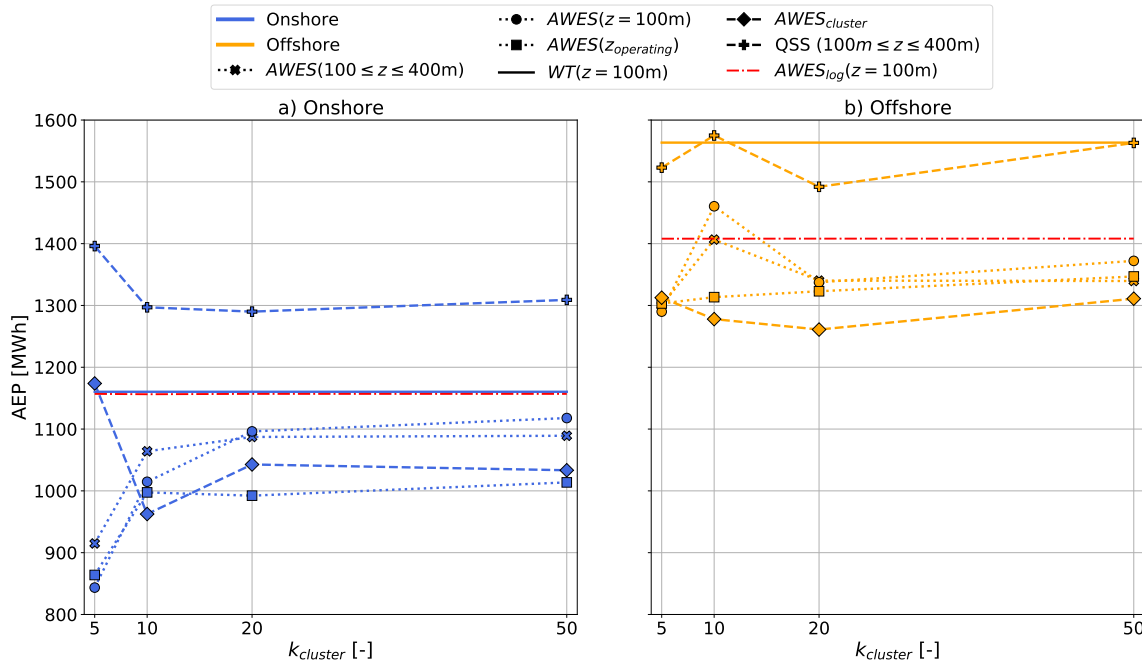


**Figure 15.** Onshore (a) and offshore (b) AEP over number of clusters  $k$  based on power curve and wind speed distribution in Sub-section 6.3 over various reference heights. QSS (+) and WT (solid lines) reference models as well as optimized AWES performance estimated based on logarithmic wind speed profiles (red dash dotted lines) and a Rayleigh distribution at 100 m.  $AWES_{cluster}$  estimates AWES AEP based on the summation of interpolated power within each cluster.

offshore results in decreased spread between reference heights. AEP predictions of  $AWES_{cluster}$  are generally lower than other estimates and closest to  $AWES(z_{operating})$ . At both locations, the QSS model over predicts AEP, due to simplified assumptions. Onshore, QSS AEP is particularly high, because tether drag might not be accurately represented, favoring higher operating altitudes. The simplified WT model predicts higher powers than the dynamic optimization AWES model, particularly offshore where lower wind shear only slightly increases energy yield at higher altitudes. Logarithmic wind speed profiles (Sub-section 5.3) and Rayleigh wind speed probability distributions ( $U_{onshore}^{ave} = 10 \text{ ms}^{-1}$  and  $U_{offshore}^{ave} = 12 \text{ ms}^{-1}$ ) also predict higher AEP than WRF-simulated wind conditions. Offshore AEP estimates based on logarithmic wind profiles are closer to power curve estimates based on WRF data than similar onshore results. This implies that offshore wind conditions (wind profile shape and probability) are better represented by logarithmic wind speed profiles than onshore conditions.

## 7 Conclusions and outlook

This study derives power-optimal, single-aircraft, ground-generation AWES trajectories and evaluates instantaneous and cycle-average power, annual energy production, operating heights and tether lengths based on representative, mesoscale simulation

570 data. These analyses use both onshore wind data at Pritzwalk in northern Germany and offshore wind data at the FINO3  
research platform in the North Sea to drive AWES optimization framework (*awebox*). These simulations span an entire year  
with a temporal resolution of 10 minutes, thereby including seasonal, synoptic and diurnal variations at a higher resolution  
than re-analysis data sets. The annual wind roses for heights of 100 m and 500 m confirm the expected wind speed increase  
and clockwise rotation at both locations, with generally lower offshore wind shear and veer than onshore. Annual wind speed  
statistics reveal that while average wind speeds increase with height, low wind speeds still occur at a fairly high probability up  
575 to 1000 m.

To further dissect wind conditions essential to the design and operation of AWES and to reduce computational cost, a repre-  
sentative wind resource model is deduced using k-means clustered wind data. This algorithm groups similar profiles together  
into a fixed, predetermined number of k clusters represented by the mean of each cluster. For a representative k of 10 (chosen  
for visualization purposes) a more extensive analysis and comparison between onshore and offshore wind conditions revealed  
580 that average wind speed, rather than profile shape, plays a decisive role in assigning profiles to a certain cluster. The algorithm  
was able to identify a cluster for onshore LLJs as well as various non-logarithmic wind profiles at both locations. Individual  
clusters produce coherent groups of similar wind velocity profiles whose probability correlates with seasonal, diurnal and at-  
mospheric stability variation. k-means clustering provides good insight into the wind regime, especially for higher altitudes  
where classification by Obukhov length is inadequate. Furthermore, the so derived clusters represent annual variation better  
585 than conventional logarithmic or exponential wind speed profiles.

Trajectories for three representative wind velocity profiles, selected based on the 5th, 50th and 95th percentile wind speed  
from each k=5,10,20,50 cluster, as well as logarithmic reference wind speed profiles, are optimized. A scaled Ampyx AP2  
aircraft ( $A_{wing} = 20 \text{ m}^2$ ) is analyzed in terms of trajectory, operating altitude, instantaneous tether force and length as well as  
power and AEP. AWESs at both locations rarely operate above 400 m, with offshore systems mostly flying below 200 m, due  
590 to higher wind speeds at lower altitude and low wind shear. These results weaken the claim of increased power harvest above  
500 m for AWES, but also obviate airspace restriction challenges for AWES. A simplified quasi-steady state (QSS) AWES as  
well as WT models are used to contextualize the optimization results and functioned as reference for power curve descriptions  
over various reference heights. The WT model reach rated power at lower wind speeds, because tether losses decrease AWES  
power, which the QSS AWES model can not fully capture. Deriving AWES power curves from logarithmic wind speed profiles  
595 seems like a valid approach especially offshore. Logarithmic wind speed profiles onshore can not account for the high amount  
of non-monotonic profiles. Onshore, the choice of reference height can seemingly result in delayed rated power as the power  
curve shifts. This choice is less significant offshore due reduced wind shear and more monotonic wind velocity profiles. This  
choice highly affects AEP predictions and requires further investigation.

Beneficial offshore wind conditions lead to higher AWES AEP than onshore. However, onshore AWES predict a higher  
600 improvement relative to the WT reference model, which generally predicts higher AEP, due to higher wind shear and higher  
wind speeds aloft. QSS AWES model AEP estimates are higher than dynamic optimization results, because they do not capture  
power variation along the flight path and under-predict tether losses. Probably the most realistic, but also lowest energy yield  
predictions are derived from wind speed distributions at operating height  $AWES_{operating}$  and the summation of annual, inter-

polated power  $AWES_{cluster}$ . AWES AEP based on logarithmic wind profiles and Rayleigh wind speed distributions predict  
605 higher yield than AEP based on clustered WRF-simulated wind resource, indicating that the conventional approach can not  
reproduce the impact of realistic wind conditions on AWES performance. This is due to the fact that the Rayleigh distribution  
over-predicts high wind speeds. Comparing WRF-clustered AEP for different power and wind resource descriptions show that  
the benefits of using more than  $k=20$  clusters are marginal while computational expense increases. Using the wind speed distri-  
bution at a fixed reference height of 100 m leads to an over prediction of annual energy, particularly onshore. We propose to use  
610 the average wind speed between 100 - 400 m, because AWES mostly operate within this range and AEP estimates are closer  
to AEP of  $AWES_{operating}$  and  $AWES_{cluster}$ . The choice of reference height for the derivation of the wind speed probability  
distribution is more important onshore, due to higher wind shear and more non-monotonic wind speed profiles.

In summary, k-means clustering provides adequate categorization and realistic, representative wind velocity profiles for  
AWES trajectory optimization. This approach increases the accuracy of AWES power prediction in comparison to logarithmic  
615 wind speed profiles. Furthermore, clustering reduces the computational cost of power curve and AEP estimates as a low  
number of clusters suffices. The choice of reference height impacts the power curve and AEP estimates, further demonstrating  
the importance of defining adequate AWES standards. Offshore AWES power curves generated based on WRF wind data are  
similar to power curves based on logarithmic reference model, because non-monotonic wind profile shapes are less common  
offshore. Estimating AEP based on wind statistics from a posteriori operating heights or from the summation of interpolated  
620 power within each cluster produces similar results. These AEP approximations need to be validated against real AWES AEP  
data.

Based on these results, we will describe the design space and weight budget of ground-generation AWES in a future sizing  
study using the clustered wind data. To that end, we will compare the performance of a high lift airfoil to the baseline AP2  
aerodynamic reference model and determine the maximum permissible mass for different wing sizes. In the end, an investiga-  
625 tion of measured power curves and real AEP from field trials is necessary to confirm or highlight deficiencies in the models  
used in this paper. Until then, long-term AWES performance analysis based on mesoscale and reanalysis data are an alternative  
to estimate AWES AEP. The simple power curve and AEP estimates presented in this research, can be compared to results  
derived from methods using more detailed numerical integration that take clustering and power optimization into account. The  
description of the AWES wind resource, particularly onshore, needs further analysis as it highly impacts AWES energy yield  
630 predictions. An interesting open research question is the seasonality of AWES performance in comparison to WT.

## 7.1 Acknowledgments and funding sources

The authors thank the BMWi for funding of the “OnKites I” and “OnKites II” project [grant number 0325394A] on the basis  
of a decision by the German Bundestag and project management Projektträger Jülich. We thank the PICS, NSERC and the  
DAAD for their funding.

635 `awebox` has been developed in collaboration with the company Kiteswarms Ltd. The company has also supported the  
`awebox` project through research funding. The `awebox` project has received funding from the European Union’s Horizon  
2020 research and innovation program under the Marie Skłodowska-Curie grant agreement No 642682 (AWESCO)

We thank the Carl von Ossietzky University of Oldenburg and the Energy Meteorology research group for providing access to their high performance computing cluster *EDDY* and ongoing support.

640 We further acknowledge Rachel Leuthold (University of Freiburg, SYSCOP) and Thilo Bronnenmeyer (Kiteswarms Ltd.) for their helped in writing this article, great, technical support and continued work on the *awebox*.

## 7.2 Author contribution

Markus Sommerfeld evaluated the data and wrote the manuscript in consultation and under the supervision of Curran Crawford. Martin Dörenkämper set up the numerical offshore simulation, contributed to the meteorological evaluation of the data and  
645 reviewed the manuscript. Jochem De Schutter co-developed the optimization model and helped writing and reviewed this manuscript.

## References

- Ampyx: Ampyx Power BV, <https://www.ampyxpowers.com/>, last accessed: 30.10.2020, 2020.
- Andersson, J. A. E., Gillis, J., Horn, G., Rawlings, J. B., and Diehl, M.: CasADi – A software framework for nonlinear optimization and  
650 optimal control, *Mathematical Programming Computation*, 11, 1–36, <https://doi.org/10.1007/s12532-018-0139-4>, 2019.
- Archer, C. L., Colle, B. A., Veron, D. L., Veron, F., and Sienkiewicz, M. J.: On the predominance of unstable atmospheric conditions in  
the marine boundary layer offshore of the U.S. northeastern coast, *Journal of Geophysical Research: Atmospheres*, 121, 8869–8885,  
<https://doi.org/10.1002/2016JD024896>, <https://agupubs.onlinelibrary.wiley.com/doi/abs/10.1002/2016JD024896>, 2016.
- Argatov, I. and Silvennoinen, R.: Efficiency of Traction Power Conversion Based on Crosswind Motion, pp. 65–79, Springer Berlin Heidel-  
655 berg, Berlin, Heidelberg, [https://doi.org/10.1007/978-3-642-39965-7\\_4](https://doi.org/10.1007/978-3-642-39965-7_4), [https://doi.org/10.1007/978-3-642-39965-7\\_4](https://doi.org/10.1007/978-3-642-39965-7_4), 2013.
- Arya, P. and Holton, J.: Introduction to Micrometeorology, International Geophysics, Elsevier Science, 2001.
- Aull, M., Stough, A., and Cohen, K.: Design Optimization and Sizing for Fly-Gen Airborne Wind Energy Systems, *Automation*, 1, 1–16,  
2020.
- Banta, R. M.: Stable-boundary-layer regimes from the perspective of the low-level jet, *Acta Geophysica*, 56, 58–87,  
660 <https://doi.org/10.2478/s11600-007-0049-8>, <https://doi.org/10.2478/s11600-007-0049-8>, 2008.
- Bronnenmeyer, T.: Optimal Control for Multi-Kite Emergency Trajectories, Master’s thesis, University of Stuttgart, <https://cdn.syscop.de/publications/Bronnenmeyer2018.pdf>, 2018.
- Carl von Ossietzky Universität Oldenburg: EDDY @ONLINE, <https://www.uni-oldenburg.de/fk5/wr/hochleistungsrechnen/hpc-facilities/eddy/>, 2018.
- 665 Cherubini, A., Papini, A., Vertechy, R., and Fontana, M.: Airborne Wind Energy Systems: A review of the technologies, *Renewable and Sustainable Energy Reviews*, 51, 1461–1476, <https://doi.org/10.1016/j.rser.2015.07.053>, <http://linkinghub.elsevier.com/retrieve/pii/S1364032115007005>, 2015.
- De Schutter, J., Leuthold, R., and Diehl, M.: Optimal Control of a Rigid-Wing Rotary Kite System for Airborne Wind Energy, in: Proceedings  
of the European Control Conference (ECC), 2018.
- 670 De Schutter, J., Leuthold, R., Bronnenmeyer, T., Paelinck, R., and Diehl, M.: Optimal control of stacked multi-kite systems  
for utility-scale airborne wind energy, in: 2019 IEEE 58th Conference on Decision and Control (CDC), pp. 4865–4870,  
<https://doi.org/10.1109/CDC40024.2019.9030026>, 2019.
- Dee, D. P., Uppala, S. M., Simmons, A. J., Berrisford, P., Poli, P., Kobayashi, S., Andrae, U., Balmaseda, M. A., Balsamo, G., Bauer,  
P., Bechtold, P., Beljaars, A. C. M., van de Berg, L., Bidlot, J., Bormann, N., Delsol, C., Dragani, R., Fuentes, M., Geer, A. J., Haim-  
675 berger, L., Healy, S. B., Hersbach, H., Hólm, E. V., Isaksen, L., Kållberg, P., Köhler, M., Matricardi, M., McNally, A. P., Monge-Sanz,  
B. M., Morcrette, J.-J., Park, B.-K., Peubey, C., de Rosnay, P., Tavolato, C., Thépaut, J.-N., and Vitart, F.: The ERA-Interim reanalysis:  
configuration and performance of the data assimilation system, *Quarterly Journal of the Royal Meteorological Society*, 137, 553–597,  
<https://doi.org/10.1002/qj.828>, 2011.
- Diehl, M.: Airborne Wind Energy: Basic Concepts and Physical Foundations, in: *Airborne Wind Energy*, edited by Ahrens, U., Diehl, M.,  
680 and Schmehl, R., pp. 3–22, Springer Berlin Heidelberg, Berlin, Heidelberg, [https://doi.org/10.1007/978-3-642-39965-7\\_1](https://doi.org/10.1007/978-3-642-39965-7_1), [https://doi.org/10.1007/978-3-642-39965-7\\_1](https://doi.org/10.1007/978-3-642-39965-7_1), 2013.
- Donlon, C. J., Martin, M., Stark, J., Roberts-Jones, J., Fiedler, E., and Wimmer, W.: The Operational Sea Surface Temperature and Sea Ice  
Analysis (OSTIA) system, *Remote Sensing of Environment*, 116, 140–158, <https://doi.org/10.1016/j.rse.2010.10.017>, 2012.



- Dörenkämper, M., Optis, M., Monahan, A., and Steinfeld, G.: On the Offshore advection of Boundary-Layer Structures and the Influence on Offshore Wind Conditions, *Boundary-Layer Meteorol.*, 155, 459–482, <https://doi.org/10.1007/s10546-015-0008-x>, 2015.
- Dörenkämper, M., Stoevesandt, B., and Heinemann, D.: Derivation of an offshore wind index for the German bight from high-resolution mesoscale simulation data, *Proceedings of DEWEK - German Offshore Wind Energy Conference*, p. 5, 2017.
- Dörenkämper, M., Olsen, B. T., Witha, B., Hahmann, A. N., Davis, N. N., Barcons, J., Ezber, Y., García-Bustamante, E., González-Rouco, J. F., Navarro, J., Sastre-Marugán, M., Sile, T., Trei, W., Žagar, M., Badger, J., Gottschall, J., Sanz Rodrigo, J., and Mann, J.: The Making of the New European Wind Atlas – Part 2: Production and evaluation, *Geoscientific Model Development*, 13, 5079–5102, <https://doi.org/10.5194/gmd-13-5079-2020>, <https://gmd.copernicus.org/articles/13/5079/2020/>, 2020.
- Echeverri, P., Fricke, T., Homsy, G., and Tucker, N.: The Energy Kite - Selected Results From the Design, Development and Testing of Makani’s Airborne Wind Turbines - Part 1, Technical Report 1, Makani Power, [https://storage.googleapis.com/x-prod.appspot.com/files/Makani\\_TheEnergyKiteReport\\_Part1.pdf](https://storage.googleapis.com/x-prod.appspot.com/files/Makani_TheEnergyKiteReport_Part1.pdf), 2020.
- Eijkelhof, D., Rapp, S., Fasel, U., Gaunaa, M., and Schmehl, R.: Reference Design and Simulation Framework of a Multi-Megawatt Airborne Wind Energy System, *Journal of Physics: Conference Series*, 1618, 032 020, <https://doi.org/10.1088/1742-6596/1618/3/032020>, <https://doi.org/10.1088/1742-6596/1618/3/032020>, 2020.
- Emeis, S.: *Wind energy meteorology: atmospheric physics for wind power generation*, Springer, Heidelberg, 2018.
- Fagiano, L. and Milanese, M.: Airborne Wind Energy: An overview, in: 2012 American Control Conference (ACC), pp. 3132–3143, <https://doi.org/10.1109/ACC.2012.6314801>, 2012.
- Floors, R., Batchvarova, E., Gryning, S.-E., Hahmann, A. N., Peña, A., and Mikkelsen, T.: Atmospheric boundary layer wind profile at a flat coastal site - wind speed lidar measurements and mesoscale modeling results, *Advances in Science and Research*, 6, 155–159, <https://doi.org/10.5194/asr-6-155-2011>, <http://www.adv-sci-res.net/6/155/2011/>, 2011.
- Gros, S., Zanon, M., and Diehl, M.: A relaxation strategy for the optimization of airborne wind energy systems, in: Control Conference (ECC), 2013 European, pp. 1011–1016, IEEE, [http://ieeexplore.ieee.org/xpls/abs\\_all.jsp?arnumber=6669670](http://ieeexplore.ieee.org/xpls/abs_all.jsp?arnumber=6669670), 2013.
- Haas, T., Schutter, J. D., Diehl, M., and Meyers, J.: Wake characteristics of pumping mode airborne wind energy systems, *Journal of Physics: Conference Series*, 1256, 012 016, <https://doi.org/10.1088/1742-6596/1256/1/012016>, <https://doi.org/10.1088/1742-6596/1256/1/012016>, 2019.
- Hahmann, A. N., Sile, T., Witha, B., Davis, N. N., Dörenkämper, M., Ezber, Y., García-Bustamante, E., González-Rouco, J. F., Navarro, J., Olsen, B. T., and Söderberg, S.: The making of the New European Wind Atlas – Part 1: Model sensitivity, *Geoscientific Model Development*, 13, 5053–5078, <https://doi.org/10.5194/gmd-13-5053-2020>, <https://gmd.copernicus.org/articles/13/5053/2020/>, 2020.
- Hersbach, H. and Dick, D.: ERA5 reanalysis is in production, <http://www.ecmwf.int/en/newsletter/147/news/era5-reanalysis-production>, last accessed: 22.10.2019, 2016.
- Houska, B. and Diehl, M.: Optimal control for power generating kites, in: 2007 European Control Conference (ECC), pp. 3560–3567, <https://doi.org/10.23919/ECC.2007.7068861>, 2007.
- HSL: The HSL Mathematical Software Library @ONLINE, <http://www.hsl.rl.ac.uk/>, 2020.
- International Electrotechnical Commission, ed.: Design requirements: amendment 1, no. 1,1 in *Wind turbines*, IEC, Geneva, ed. 3.0, 2010-10 edn., oCLC: 838280539, 2010.
- Kruijff, M. and Ruitkamp, R.: A Roadmap Towards Airborne Wind Energy in the Utility Sector, pp. 643–662, Springer Singapore, Singapore, [https://doi.org/10.1007/978-981-10-1947-0\\_26](https://doi.org/10.1007/978-981-10-1947-0_26), [https://doi.org/10.1007/978-981-10-1947-0\\_26](https://doi.org/10.1007/978-981-10-1947-0_26), 2018.

- Leuthold, R., De Schutter, J., Malz, E. C., Licitra, G., Gros, S., and Diehl, M.: Operational Regions of a Multi-Kite AWE System, in: 2018 European Control Conference (ECC), pp. 52–57, <https://doi.org/10.23919/ECC.2018.8550199>, 2018.
- Leuthold, R., De Schutter, J., Malz, E., Licitra, G., Bronnenmeyer, T., Gros, S., and Diehl, M.: *awebox*: Modelling and optimal control of single- and multiple-kite systems for airborne wind energy, <https://github.com/awebox>, 2020.
- 725 Licitra, G., Koenemann, J., Bürger, A., Williams, P., Ruitkamp, R., and Diehl, M.: Performance assessment of a rigid wing Airborne Wind Energy pumping system, *Energy*, 173, 569–585, <https://doi.org/10.1016/j.energy.2019.02.064>, 2019.
- Loyd, M. L.: Crosswind kite power (for large-scale wind power production), *Journal of energy*, 4, 106–111, <http://arc.aiaa.org/doi/abs/10.2514/3.48021>, 1980.
- Lunney, E., Ban, M., Duic, N., and Foley, A.: A state-of-the-art review and feasibility analysis of high altitude wind power in Northern Ireland, *Renewable and Sustainable Energy Reviews*, 68, 899 – 911, <https://doi.org/https://doi.org/10.1016/j.rser.2016.08.014>, <http://www.sciencedirect.com/science/article/pii/S1364032116304282>, 2017.
- 730 Malz, E., Koenemann, J., Sieberling, S., and Gros, S.: A reference model for airborne wind energy systems for optimization and control, *Renewable Energy*, 140, 1004 – 1011, <https://doi.org/https://doi.org/10.1016/j.renene.2019.03.111>, <http://www.sciencedirect.com/science/article/pii/S0960148119304239>, 2019.
- 735 Malz, E., Hedenus, F., Göransson, L., Verendel, V., and Gros, S.: Drag-mode airborne wind energy vs. wind turbines: An analysis of power production, variability and geography, *Energy*, 193, 116765, <https://doi.org/https://doi.org/10.1016/j.energy.2019.116765>, <http://www.sciencedirect.com/science/article/pii/S0360544219324600>, 2020.
- Molina-García, A., Fernández-Guillamón, A., Gómez-Lázaro, E., Honrubia-Escribano, A., and Bueso, M. C.: Vertical Wind Profile Characterization and Identification of Patterns Based on a Shape Clustering Algorithm, *IEEE Access*, 7, 30890–30904, <https://doi.org/10.1109/ACCESS.2019.2902242>, 2019.
- 740 Nakanishi, M. and Niino, H.: Development of an Improved Turbulence Closure Model for the Atmospheric Boundary Layer, *Journal of the Meteorological Society of Japan*, 87, 895–912, <https://doi.org/10.2151/jmsj.87.895>, 2009.
- Obukhov, A. M.: Turbulence in an atmosphere with a non-uniform temperature, *Boundary-Layer Meteorology*, 2, 7–29, <https://doi.org/10.1007/BF00718085>, 1971.
- 745 Olauson, J.: ERA5: The new champion of wind power modelling?, *Renewable Energy*, 126, 322–331, <https://doi.org/10.1016/j.renene.2018.03.056>, 2018.
- Optis, M., Monahan, A., and Bosveld, F. C.: Limitations and breakdown of Monin–Obukhov similarity theory for wind profile extrapolation under stable stratification, *Wind Energy*, 19, 1053–1072, <https://doi.org/10.1002/we.1883>, 2016.
- Peña, A., Gryning, S.-E., and Floors, R.: Lidar observations of marine boundary-layer winds and heights: a preliminary study, *Meteorologische Zeitschrift*, 24, 581–589, <https://doi.org/10.1127/metz/2015/0636>, [http://www.schweizerbart.de/papers/metz/detail/24/84892/Lidar\\_observations\\_of\\_marine\\_boundary\\_layer\\_winds\\_?af=crossref](http://www.schweizerbart.de/papers/metz/detail/24/84892/Lidar_observations_of_marine_boundary_layer_winds_?af=crossref), 2015.
- 750 Pedregosa, F., Varoquaux, G., Gramfort, A., Michel, V., Thirion, B., Grisel, O., Blondel, M., Prettenhofer, P., Weiss, R., Dubourg, V., Vanderplas, J., Passos, A., Cournapeau, D., Brucher, M., Perrot, M., and Duchesnay, E.: Scikit-learn: Machine Learning in Python, *Journal of Machine Learning Research*, 12, 2825–2830, 2011.
- 755 Salvação, N. and Guedes Soares, C.: Wind resource assessment offshore the Atlantic Iberian coast with the WRF model, *Energy*, 145, 276 – 287, <https://doi.org/https://doi.org/10.1016/j.energy.2017.12.101>, <http://www.sciencedirect.com/science/article/pii/S0360544217321448>, 2018.

- Schelbergen, M., Kalverla, P. C., Schmehl, R., and Watson, S. J.: Clustering wind profile shapes to estimate airborne wind energy production, *Wind Energy Science*, 5, 1097–1120, <https://doi.org/10.5194/wes-5-1097-2020>, <https://wes.copernicus.org/articles/5/1097/2020/>, 2020a.
- 760 Schelbergen, M., Kalverla, P. C., Schmehl, R., and Watson, S. J.: Clustering wind profile shapes to estimate airborne wind energy production, *Wind Energy Science Discussions*, 2020, 1–34, <https://doi.org/10.5194/wes-2019-108>, <https://www.wind-energ-sci-discuss.net/wes-2019-108/>, 2020b.
- Schmehl, R., Noom, M., and van der Vlugt, R.: Traction Power Generation with Tethered Wings, pp. 23–45, Springer Berlin Heidelberg, Berlin, Heidelberg, [https://doi.org/10.1007/978-3-642-39965-7\\_2](https://doi.org/10.1007/978-3-642-39965-7_2), [https://doi.org/10.1007/978-3-642-39965-7\\_2](https://doi.org/10.1007/978-3-642-39965-7_2), 2013.
- 765 Sempreviva, A. M. and Gryning, S.-E.: Humidity fluctuations in the marine boundary layer measured at a coastal site with an infrared humidity sensor, *Boundary-Layer Meteorology*, 77, 331–352, <https://doi.org/10.1007/BF00123531>, 1996.
- Skamarock, W., Klemp, J., Dudhia, J., Gill, D., Barker, D., Duda, M., Huang, X., Wang, W., and Powers, J.: A description of the advanced research WRF version 3, Tech. Rep. NCAR/TN–475+STR, NCAR - National Center for Atmospheric Research, Boulder, Colorado, USA, <http://n2t.net/ark:/85065/d72n51q1>, 2008.
- 770 Skamarock, W. C., Klemp, J. B., Dudhia, J., and Gill, D. O.: A Description of the Advanced Research WRF Model Version 3, Technical Report, UCAR, <https://doi.org/10.5065/D68S4MVH>, a.
- Skamarock, W. C., Klemp, J. B., Dudhia, J., and Gill, D. O.: Github: Weather Research and Forecasting Model, <https://github.com/wrf-model/WRF/releases>, b.
- Skamarock, W. C., Klemp, J. B., Dudhia, J., and Gill, D. O.: A Description of the Advanced Research WRF Model Version 4.3, Technical Report, UCAR, <https://doi.org/10.5065/1dfh-6p97>, c.
- 775 Sommerfeld, M., Crawford, C., Monahan, A., and Bastigkeit, I.: LiDAR-based characterization of mid-altitude wind conditions for airborne wind energy systems, *Wind Energy*, 22, 1101–1120, <https://doi.org/10.1002/we.2343>, 2019a.
- Sommerfeld, M., Dörenkämper, M., Steinfeld, G., and Crawford, C.: Improving mesoscale wind speed forecasts using lidar-based observation nudging for airborne wind energy systems, *Wind Energy Science*, 4, 563–580, <https://doi.org/10.5194/wes-4-563-2019>, [https://www.](https://www.wind-energ-sci.net/4/563/2019/)
- 780 [wind-energ-sci.net/4/563/2019/](https://www.wind-energ-sci.net/4/563/2019/), 2019b.
- Stull, R.: *An Introduction to Boundary Layer Meteorology*, Atmospheric and Oceanographic Sciences Library, Springer Netherlands, <https://books.google.ca/books?id=eRRz9RNvNOKC>, 1988.
- van der Vlugt, R., Bley, A., Noom, M., and Schmehl, R.: Quasi-steady model of a pumping kite power system, *Renewable Energy*, 131, 83–99, <https://doi.org/10.1016/j.renene.2018.07.023>, <http://www.sciencedirect.com/science/article/pii/S0960148118308206>, 2019.
- 785 Waechter, A. and Laird, C.: Ipopt (Interior Point OPTimizer), <https://github.com/coin-or/Ipopt>, 2016.
- Wächter, A. and Biegler, L. T.: On the implementation of an interior-point filter line-search algorithm for large-scale nonlinear programming, *Mathematical Programming*, 106, 25–57, <https://doi.org/10.1007/s10107-004-0559-y>, <https://doi.org/10.1007/s10107-004-0559-y>, 2006.

## Appendix A: Figures

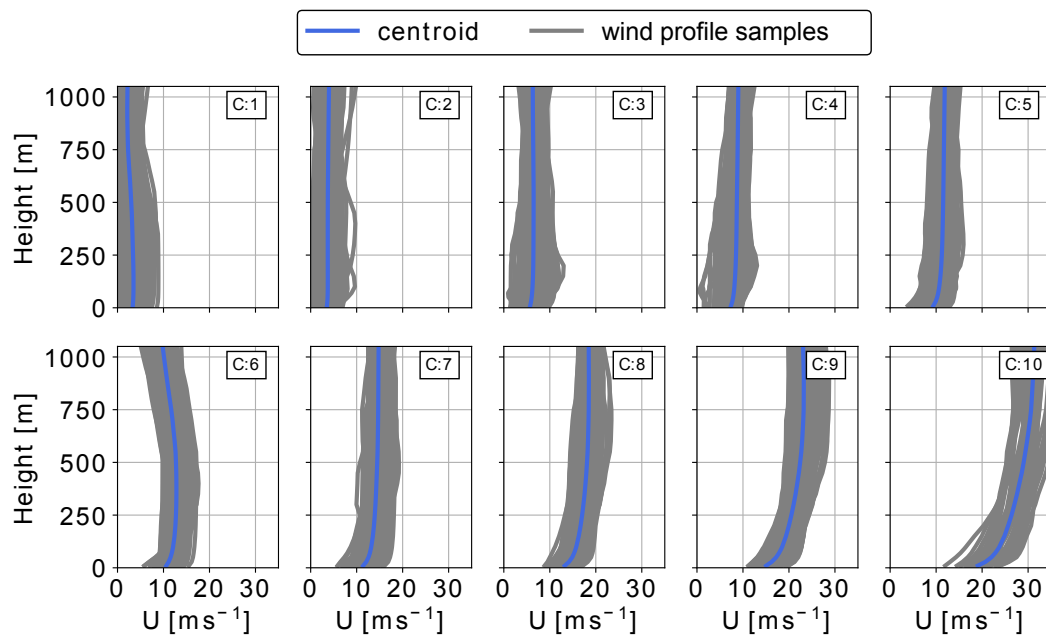


**Figure A1.** clustered offshore wind velocity profiles (here shown as 2D projected wind speed profiles). The average profile or centroid is shown in blue while all the assigned profiles are shown in grey.

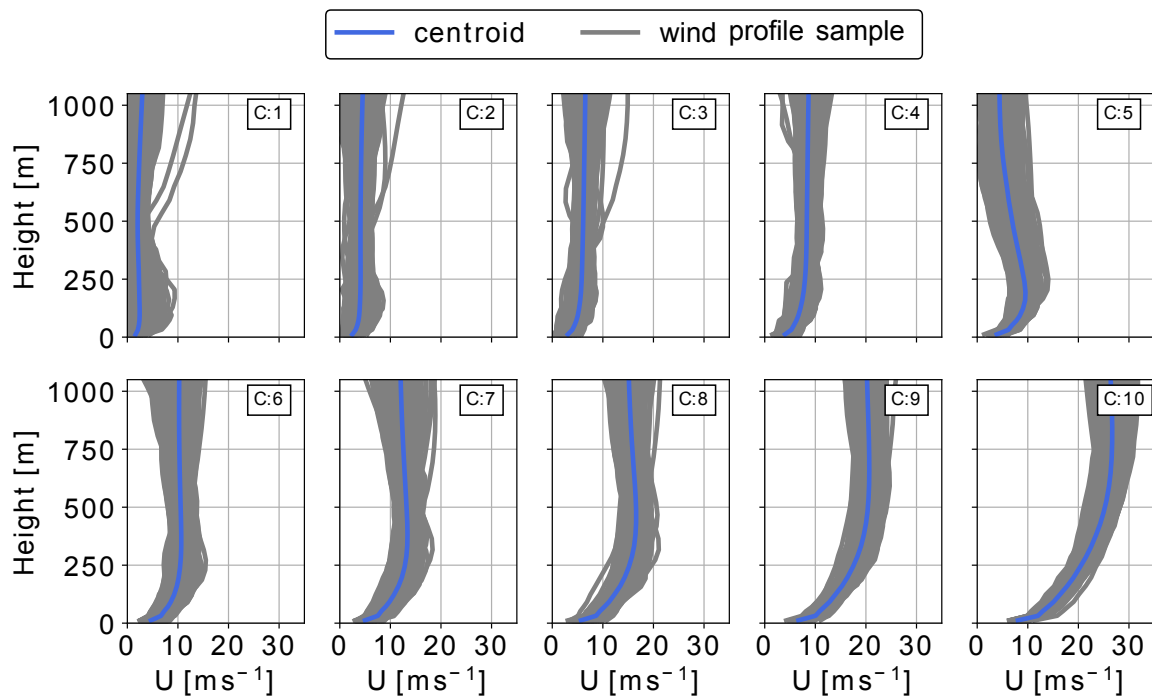


**Figure A2.** Clustered onshore wind velocity profiles (here shown as wind speed profiles). The average profile or centroid is shown in blue while all the assigned profiles are shown in grey.

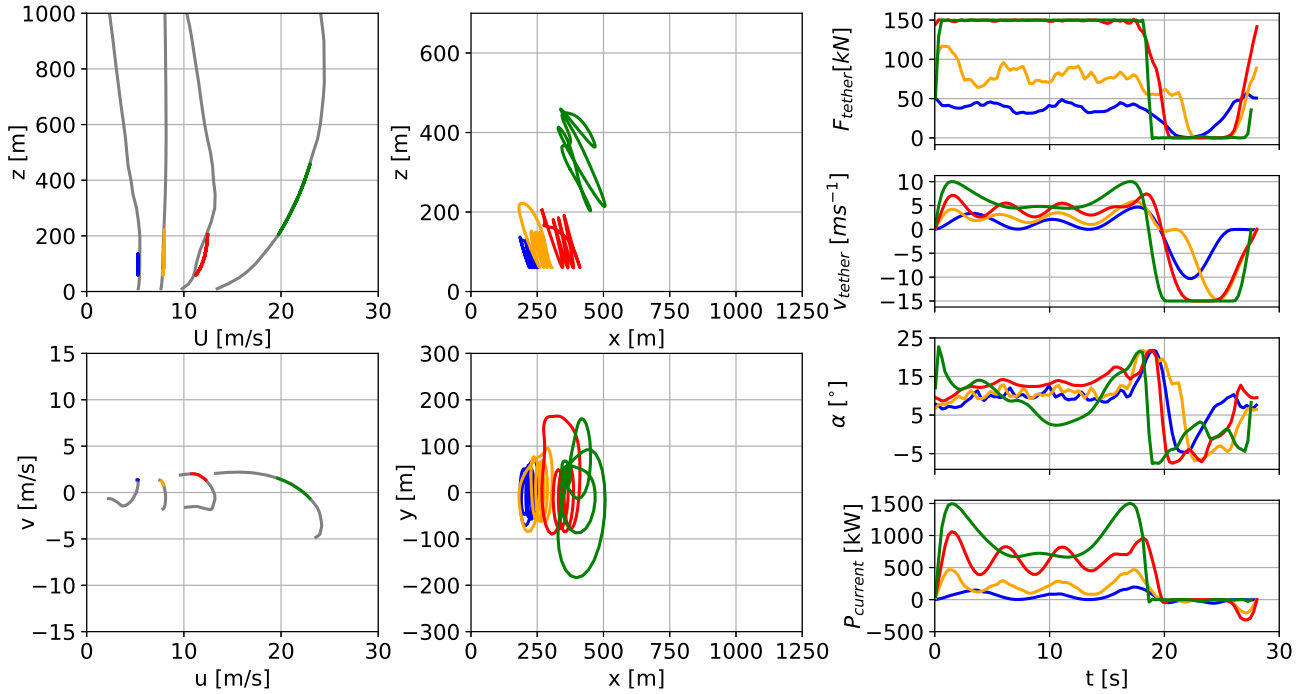


**Figure A3.** Representative wind speed profiles (a), and hodograph (top view) of wind velocity up to 1000 m (c). The deviation of the colored lines is caused by the approximation of discrete data points with Lagrange polynomials. Trajectories (b,d) in side and top view. Temporal variations of tether force  $F_{\text{tether}}$  (e), tether speed  $v_{\text{tether}}$  (f), angle of attack  $\alpha$  (g) and instantaneous power  $P_{\text{current}}$  (h) optimized based on clustered offshore wind speed profiles for a ground-generation aircraft with a wing area of  $A_{\text{wing}} = 20 \text{ m}^2$ .